Capillarity in Complicated Geometries

by

Mohammad Amin Zakershobeiri

B.Sc., Amirkabir University of Technology, 2018

A THESIS SUBMITTED IN PARTIAL FULFILLMENT OF
THE REQUIREMENTS FOR THE DEGREE OF

MASTER OF APPLIED SCIENCE

in

The Faculty of Graduate and Postdoctoral Studies

(Mechanical Engineering)

THE UNIVERSITY OF BRITISH COLUMBIA

(Vancouver)

October 2021

The following individuals certify that they have read, and recommend to the Faculty of Graduate and Postdoctoral Studies for acceptance, the thesis entitled:

Capillarity in Complicated Geometries

submitted by Mohammad Amin Zakershobeiri in partial fulfillment of the requirements for

the degree of Master of Applied Science

in Mechanical Engineering

Examining Committee:

Mauricio Ponga, Mechanical Engineering, UBC
Supervisor

Gwynn Elfring, Mechanical Engineering, UBC
Supervisory Committee Member

Mark Martinez, Chemical and Biological Engineering, UBC
Supervisory Committee Member

Abstract

In this thesis, a novel visco-inertial formulation of capillarity is proposed that geometrically extends the Bosanquet equation to irregular geometries, taking the effect of inertia and the dynamic contact angle into account. The governing equation is an integro-differential equation that is solved numerically and compared with computer simulations, experimental data, and other cases available in the literature. The numerical examples investigated in this work show that contrary to flat channels and tubes, inertial effects decay much slower in corrugated channels and tubes due to the walls' geometrical fluctuations. Most importantly, it will be shown that the true solution for Jurin's height in irregular capillaries is *path-dependent* and highly sensitive to the initial conditions, and no single static-equilibrium solution can necessarily be attributed to the eventual position of the meniscus. Resulting from the non-linear dynamics, the multiple equilibria in the presence of gravity for irregular capillaries can only be analyzed if the effect of inertia is considered, which has largely been neglected in the literature thus far.

Lay Summary

Capillarity is a ubiquitous phenomenon in nature with great applications in medicine and engineering. Although a myriad of studies have investigated capillarity for centuries, they usually come with the simplification of the geometry or the physics involved. The literature was lacking in a study considering the effect of inertia in irregular capillaries (other than wicking in simple straight tubes or between parallel plates). In this regard, this thesis aims at deriving a novel visco-inertial formulation for capillarity in complicated geometries.

Preface

This thesis entitled *"capillarity in complicated geometries"* presents the original, unpublished, and independent work of the author, Mohammad Amin Zakershobeiri (Amin Shobeiri) under the supervision of Dr. Mauricio Ponga over the course of a Master of Applied Science (MASc) program at UBC Mechanical Engineering.

The theory developed in Chapter 3 and parts of the results presented in Chapter 4 are under peer-review for academic publication at the time of writing this manuscript.

Table of Contents

Abstract iii

Lay Summary iv

Preface v

Table of Contents vi

List of Tables ix

List of Figures x

Nomenclature xiii
Latin Letters xiv
Greek Letters xvi
Subscripts and Superscripts xvii
Abbreviations xviii

Acknowledgements xix

Dedication xx

1 Introduction 1
1.1 Capillary Phenomena 1
1.2 Young-Laplace Equation 2
1.3 Jurin's Height 2
1.4 Washburn's Theory 4
1.5 Bosanquet's Theory 5
1.6 Irregular Capillaries 6
1.7 Numerical Simulation of Capillarity 9
1.8 Thesis Outline 10

2 Problem Statement . . . 12
2.1 Rectification of Tortuous Channels and Tubes . . . 13
2.1.1 Centerline Determination . . . 14
2.1.2 Voronoi Segmentation . . . 14
2.2 Correction of the Hagen–Poiseuille Equation in Corrugated Channels . . . 15

3 Analysis . . . 20
3.1 Reynolds Transport Theorem . . . 20
3.2 Expansion of the Terms . . . 25
3.2.1 Moving Boundary Term . . . 25
3.2.2 Flux Term . . . 26
3.2.3 Viscous Term . . . 26
3.2.4 Pressure Term . . . 27
3.2.5 Gravity Term . . . 28
3.3 Governing ODE . . . 28

4 Results and Discussions . . . 31
4.1 Verification with Computational Fluid Dynamics . . . 31
4.1.1 Grid Independence and Meshing Considerations . . . 32
4.1.2 Time Step Independence: . . . 32
4.1.3 Domain Independence . . . 32
4.2 Validation of the VOF . . . 33
4.3 Results . . . 34
4.3.1 Lower Reynolds Results . . . 35
4.3.2 Higher Reynolds Results . . . 42
4.3.3 Effect of Gravity . . . 42
4.3.4 Tubular Geometries . . . 44
4.4 Discussion . . . 46
4.4.1 Dominant Forces during Capillary Rise . . . 47
4.4.2 Jurin's Height . . . 48

5 Conclusions and Future Work . . . 56

Bibliography . . . 59

Appendices . . . 67

A Force Balance . . . 67

B Differential Element Stretch Rate . . . 68

C Dynamic Contact Angle 70

D Convergence Study 72
D.1 Mesh Convergence 72
D.2 Domain Convergence 72

List of Tables

1.1 Some frequently used non-dimensional numbers in the literature, Re, Oh, and Bond numbers in relevant capillarity problems together with the viscous (t_v) and capillary (t_c) time scales. 6

4.1 The geometrical and flow specifications of 6 cases studied and verified against VOF simulation. 41
4.2 Water properties at 15°C and 20°C. 51

D.1 Mesh convergence study, four mesh configuration with ordered by the refinement increase tabulated with the height of the meniscus at $t = 0.5$ s. 72
D.2 Domain convergence study, three domains with as same refinement as the obtained reliable mesh (M3) in descending order indicated by the normalized distance to the centerline of the capillary, tabulated with the height of the meniscus at $t = 0.5$ s. 73

List of Figures

1.1 The occurrences and applications of capillarity in nature ((a), (b)), medicine (c), and engineering ((d), (e)). 3
1.2 Geometric dependence of the meniscus configuration on the wall angle (β) and (a) the width of a channel ($h(s)$) and (b) the radius of the tube ($r(s)$) at the meniscus ($s = L$). 8

2.1 Schematic of the rectification process for tortuous periodic (a) channels and (b) tubes. 17
2.2 The comparison of the average and Voronoi centerlines in for types of sinusoidal channels, (a) anti-symmetric ($\psi = 0$), (b) shifted at $\psi = \pi/3$, (c) shifted at $\psi = 2\pi/3$. 18
2.3 The viscous correction factor (ξ) plotted against $\zeta = \varepsilon \mathrm{Re}$ in a bilogarithmic scale, estimated by $(1 + 0.085\,\zeta)^{-1}$ 19

3.1 A schematic of the problem, (a) a corrugated and tortuous channel (2D) exposed to a liquid reservoir represented with (a) the magnified meniscus configuration, (b) a generic volume element with the corresponding dimensions, and (c) acting stresses and incoming and outgoing velocities. 23

4.1 The outlook of the VOF simulations, (a) shows multiple snapshots of the capillary rise in a sample case (Figure 4.3(c)) over time. (b) demonstrates the spatial discretization of the domain through structured meshing in the same symmetric geometry, and (c) shows the structured mesh grid in a tortuous channel. 37
4.2 Comparing the VOF simulation results to the experimental data published by Stange *et al.*. 38

4.3 Wicking length ($L(t)$) and rate ($\dot{L}(L)$) results in lower Reynolds range ($\mathrm{Re} \sim 30 - 40$) for the extended Washburn, extended Bosanquet (with $\gamma(t) = 1$), and extended Bosanquet + DCA compared against VOF simulations in three sinusoidal capillaries, (a) case 1, anti-symmetric ($\psi = 0$), (c) case 2, shifted at $\psi = \pi/4$, (e) case 3, symmetric ($\psi = \pi$). 39
4.4 Wicking length ($L(t)$) and rate ($\dot{L}(L)$) results in higher Reynolds range ($\mathrm{Re} \sim 50 - 70$) for the extended Washburn, extended Bosanquet (with $\gamma(t) = 1$), and extended Bosanquet + DCA compared against VOF simulations in three sinusoidal capillaries, (a) case 1, anti-symmetric ($\psi = 0$), (c) case 2, shifted at $\psi = \pi/4$, (e) case 3, symmetric ($\psi = \pi$). 40
4.5 The effect of gravity on the capillary rise of water in a tortuous and corrugated channel. Two cases with the same geometry are represented with a downward ($g = 9.81\ \mathrm{m \cdot s^{-2}}$) and zero gravity. The case with the downward gravity achieves equilibrium at the Jurin's height ($L_J = 12.3$ mm) after slight gravitational oscillations. 43
4.6 (a) Comparison between the extended Bosanquet equation and extended Washburn equation and the results obtained by Erickson *et al.* using interface-tracking solution on a pair of symmetric converging-diverging and diverging-converging stepped-tubes. Three special regions of interest (I, II, and III) are magnified in (b) to clearly distinguish between different sets of results. 45
4.7 The share of terms in the total magnitude over time, $\mathcal{M}(t)$, plotted in a semi-logarithmic scale for the wicking of water in a channel. (a) and (c) represent a flat channel, while (b) and (d) show the share of terms for a sinusoidal symmetric corrugated channel with the. The gravity is present in (a) and (b) ($g = 1\ \mathrm{m \cdot s^{-2}}$), but not (c) and (d). 49
4.8 The multiple static equilibria plotted as a function of the meniscus position (L) for a sinusoidal symmetric channel. The stable (Jurin's heights) and unstable equilibria are presented with up-pointing and down-pointing triangles, respectively. The derivative of $P_c - P_g$ at the equilibria signifies stability once negative, and vice versa. 50

4.9 The effect of dynamic viscosity (η) on the Jurin's height in a sinusoidal symmetric channel. (a) shows the Jurin's height for few sample viscosities in two intervals of $\eta > 0.00128$ kg·m^{-1}·s^{-1} and $0.00127 > \eta > 0.00032$ kg·m^{-1}·s^{-1}. The bifurication occurs between $0.00128 > \eta > 0.00127$ kg·m^{-1}·s^{-1}, where the curves part at an unstable equilibrium height, $L = 9.2$ mm. (b) covers the interval of $0.00031 > \eta > 0$ kg·m^{-1}·s^{-1}, showing multiple Jurin's height due to relative stronger effect of inertia. 52
4.10 The capillary rise of water in a sinusoidal symmetric channel at two different temperatures (15°C and 20°C). The small difference in water properties just by a 5°C temperature causes the meniscus to eventually come to rest in different stable equilibria. 53
4.11 The effect of the initial condition (L_0) on the the Jurin's height of water in a sinusoidal symmetric channel. 54

B.1 The schematic of the integral discretization as the summation of finite elements. 68

C.1 Several snapshots from the early stages of meniscus formation in a silicone fluid (SF). 70
C.2 The evolution of the dynamic contact angle model $\gamma(t)$ over time in a semi-logarithmic plot. 71

Nomenclature

Latin Letters

Symbol	Description	SI Unit
a	corrugation amplitude	m
A	cross-sectional area	m^2
$\mathcal{A}$	first inertial ODE coefficient	$kg.m^{-2}$
b	breadth or 2D depth of a channel	m
$\mathcal{B}$	second inertial ODE coefficient	$kg.m^{-3}$
Bo	Bond number	[–]
c	centerline function	m
$\mathcal{C}$	viscous ODE coefficient	$kg.s^{-1}.m^{-2}$
D	diameter	m
$\mathcal{D}$	capillary term of the ODE	Pa
De	Dean number	[–]
$\hat{\mathbf{e}}$	unit vector	[–]
F	force	N
g	gravitational acceleration	$m.s^{-2}$
$\mathcal{G}$	gravity term of the ODE	Pa
h	width	m
H	dynamic contact angle *ad hoc* constant	m
L	wicking length	m
ℓ	normal to arclength coordinate (s) in 2D	m
$\mathcal{M}$	total magnitude	Pa
Oh	Ohnesorge number	[–]

Latin Letters: *continued*

Symbol	Description	SI Unit
P	pressure	Pa
p	perimeter	m
Q	volumetric flow rate	$m^3.s^{-1}$
r	radius	m
R	normal to arclength coordinate (s) in 3D	m
Re	Reynolds number	[–]
s	arclength coordinate	m
t	time	s
u	velocity field	$m.s^{-1}$
$\overline{u}$	average velocity over the cross-section	$m.s^{-1}$
x	height coordinates	m
y	normal to height coordinates	m

Greek Letters

Symbol	Description	SI Unit
α	centerline angle, $\hat{\mathbf{e}}_x \cdot \hat{\mathbf{e}}_s$	rad
β	wall angle	rad
γ	dynamic contact angle exponential saturation function	[–]
ε	corrugation number	[–]
ζ	εRe	[–]
η	dynamic viscosity	$\mathrm{kg.m^{-1}.s^{-1}}$
θ	the contact angle of solid-liquid interface	rad
κ	curvature	$\mathrm{m^{-1}}$
λ	wavelength	m
ν	kinematic viscosity	$\mathrm{m^2.s^{-1}}$
ξ	viscous correction factor	[–]
ρ	mass density	$\mathrm{kg.m^{-3}}$
σ	interfacial surface tension	$\mathrm{N.m^{-1}}$
τ	shearing stress	Pa
$\boldsymbol{\tau}$	tortuosity	[–]
ϕ	square velocity average coefficient	[–]
ψ	phase shift of periodic channel walls	rad

Subscripts and Superscripts

Symbol	Description
0	initial, evaluated at $t = 0$
*	immersed below the reservoir surface
atm.	atmospheric
c	capillary
cen.	of centerline
CFD	obtained from CFD
cyl.	of a cylinder
dyn.	dynamic
g	gravitational or hydrostatic
h	hydraulic
H–P	obtained from Hagen–Poiseuille equation
i	inertial
J	Jurin's
l	left
r	right
sph.	of a sphere
v	viscous
w	wall
x	evaluated based on the height coordinate

Abbreviations

2D	2 Dimensional
3D	3 Dimensional
BCLW	Bell–Cameron–Lucas–Washburn
CFD	Computational Fluid Dynamics
CFL	Courant–Friedrichs–Lewy
DCA	Dynamic Contact Angle
Ex.	extended
H–P	Hagen–Poiseuille
ODE	Ordinary Differential Equation
VOF	Volume of Fluid

Acknowledgements

First and foremost, my immense gratitude to Dr. Mauricio Ponga for his insight, guidance, and continuous support throughout my masters program, without it this thesis would not have been completed. I am particularly grateful to him for giving me time and academic freedom to explore new ideas, try different ways, and think independently.

Many thanks to the committee members, Dr. Mark Martinez and Dr. Gwynn Elfring, for reading this document, assessing my work, and their helpful feedback.

I would like to thank all my dear friends and lab mates, Farid, Lucas, David, Mohamed, Mewael, and Reza with whom I enjoyed invaluable moments of company and conversation which truly made this journey a memorable experience. I am specially indebted to Mouad Boudina for proofreading my submitted manuscript and providing priceless advice on my research and presentation skills.

Special regards to the people at Sea-to-Sky Energy Solutions, Peter Zell, Brett Robinson, Simon Szoke, and Andreas Avgoysti, with whom I was involved in an industrial project at the beginning of my program which eventually culminated in a patent application. It was truly a splendid experience for me which I could not ever imagine.

The most important of all, I am sincerely thankful to my family, my parents and my younger brother, Matin, who provided me with their loving support.

To all those lives lost to COVID-19.

Chapter 1

Introduction

1.1 Capillary Phenomena

The spontaneous wicking or imbibition of liquids into pores, ducts, or intergranular spaces owing to the surface tension action is regarded as capillary flow [1]. It could happen upon the exposition of either a liquid-gas or an immiscible liquid-liquid interface to a solid surface [2]. Capillarity is a ubiquitous phenomenon with a wide range of occurrences and applications in nature, medicine, common industries, and state-of-the-art technologies.

Sap ascent in xylem tubes [3] (Figure 1.1(a)), passive water collection by the skin and leaves of desert fauna and flora [4–6], drinking strategies in hummingbirds' (Figure 1.1(b)), sunbirds', and honeyeaters' tongue [7–9], and water retention and transport by sandgrouse [10] all constitute occurrences of biocapillarity in nature. Moreover, some studies show that capillary force might contribute to gecko's adhesion mechanism [11, 12].

Capillarity-driven separation of blood plasma (Figure 1.1(c)) is a crucial application in medicine [13–15]. The viscosity of bodily fluids is an important indicator of a person's health and thereby crucial to medical diagnosis. As a result, capillary viscometers are extensively used to measure the viscosity of blood and other bodily fluids via their wicking pace in a capillary [16, 17].

Capillary-inspired devices are growing more and more fashionable in many engineering applications for their relative simplicity, low cost, and passiveness, especially in the field of microfluidics [9]. Paper towel and sponge absorption mechanism (Figure 1.1(d) and (e)) [18, 19], absorbent fabrics [20], spontaneous oil recovery in hydrocarbon reservoirs [21], soil sorptivity [22–24], micro-decorated surfaces [12, 25], fluid management in outer space [26, 27], catalysis [28], ink-jet printing [29], and self-lubrication [30] are only few of many common or sophisticated industrial applications of capillarity. Inverse capillary filling problem is also a method that is used to evaluate

the inner profile of very thin ducts from the experimental data of meniscus[1] progression within the capillary [31].

The motivation of this study was also initially fueled by bioproducts and systems with complex physics with occurrences and applications in nature and engineering. However, the existing literature on capillarity theories were majorly on overly simplified geometries which cannot represent complicated geometries observed in reality. In this regard, this work aims at improving the capillary theories of complicated geometries to be used for providing new insight into complex biophysics and industrial problems.

1.2 Young-Laplace Equation

The Young-Laplace equation, derived from the works of Pierre de Laplace[2] and Thomas Young[3] in 1805 [32, 33], relates the pressure difference on both sides of an immiscible fluid-fluid interface (P_c) to the total curvature of the surface (κ) and the surface tension in the interface (σ) as,

$$P_c = \kappa\sigma. \tag{1.1}$$

The total curvature of the surface is the sum of its principal curvatures. Equation 1.1 can be written as $P_c = \sigma/r_{\text{cyl.}}$ for a cylindrical and $P_c = 2\sigma/r_{\text{sph.}}$ for a spherical surface; with $r_{\text{cyl.}}$ and $r_{\text{sph.}}$ representing the radius of a cylindrical and a spherical surface, respectively. When introduced to a duct, the formation of the meniscus results in a pressure drop which drives a flow inside it; and the pressure difference P_c is often called *capillary* pressure.

1.3 Jurin's Height

In early 18TH century, Jurin[4] described the final height of the capillary rise in equilibrium in the presence of gravity (denoted with L_J) for a tube

[1] Meniscus is Greek for *crescent*, as the curved interface in a capillary is reminiscent of a crescent Moon.

[2] Pierre-Simon Marquis de Laplace (1749-1827), the prolific French polymath.

[3] Thomas Young (1773-1829), British polymath, also known for Young's modulus in solid mechanics.

[4] James Jurin (1684-1750), British physicist and physician.

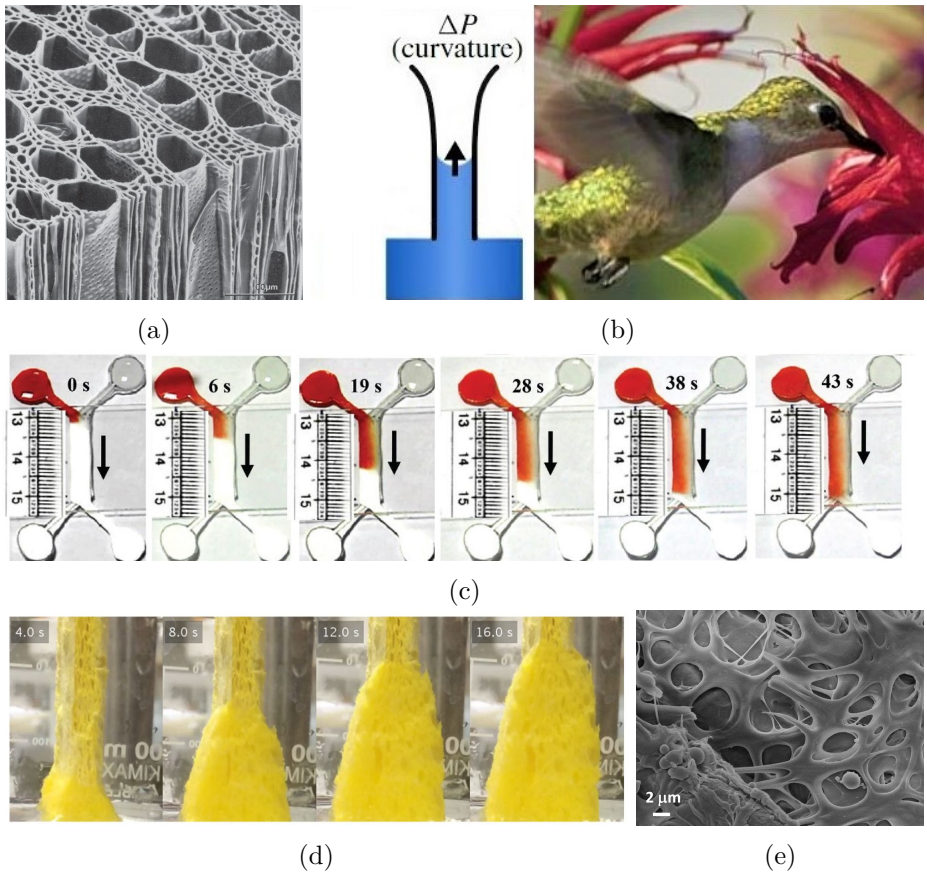

Figure 1.1: The occurrences and applications of capillarity in nature ((a), (b)), medicine (c), and engineering ((d), (e)). (a) shows a parallel array of xylems in a block of wood (reprinted from [3] with permission from © Springer-Verlag Berlin Heidelberg 1983). (b) demonstrates the eating mechanism of the hummingbird's tongue, a curvature-driven (capillary) liquid collection mechanism in animals (reprinted from [8] by © Cambridge University Press 2012). (c) real-time snapshots from the wicking of the blood (red) and a *buffer* liquid (transparent) into a paper channel, resulting in the plasma separation at the end of the channel (reprinted from [13] with permission from the © Royal Society of Chemistry 2015). (d) depicts the several stages of imbibition in a sponge over time, also causing lateral swelling (reprinted with permission from [18] © by the American Physical Society 2017), while (e) shows the micro-structure of a sponge, a typical porous medium (reprinted from [19], licensed CC-BY 4.0).

[34, 35] without the knowledge of the Young-Laplace equation. However, it can be obtained by balancing the capillary pressure in Equation 1.1 with the hydrostatic pressure $P_g = \rho g L_J$, where ρ is the mass density of the wicking liquid, g is the gravitational acceleration, and L_J is the length of capillary rise within the channel in static equilibrium. Jurin's height for a flat channel (2D) with the constant width of h may similarly be calculated and is presented alongside a simple straight tube (3D, axisymmetric) with a constant radius of r, respectively below,

$$L_J = \frac{2\sigma\cos(\theta)}{\rho g h} \qquad \text{(2D)}, \tag{1.2a}$$

$$L_J = \frac{2\sigma\cos(\theta)}{\rho g r} \qquad \text{(3D)}, \tag{1.2b}$$

where θ is the air-liquid interface contact angle with the capillary wall in equilibrium.

1.4 Washburn's Theory

Bell and Cameron observed that the height of capillary rise inside a tube is proportional to the square root of the time $L \propto \sqrt{t}$ [36]. Later, Lucas and Washburn were the first to formulate the dynamics of the capillary rise as a square-root relation $L = \sqrt{Dt}$ by describing the diffusion coefficient (D) as a function of liquid and capillary properties [37, 38]. Hence, this *quasi-steady*[5] solution is usually referred to as the *Washburn's law* or the diffusive capillary regime [39]. Although we acknowledge this theory as the collective result of the works of Bell, Cameron, Lucas, and Washburn (also known as BCLW imbibition in the literature to show the chronological contribution order [18, 39]), it is to be called Washburn's equation hereinafter in this work. Washburn's solution is presented for both parallel plates (2D) and a tube (3D), respectively below,

[5] A quasi-steady or quasi-static formulation is any static analysis of a moving system neglecting the effect of inertia due to small rate of change of properties as the system evolves in time.

$$\dot{L} = \frac{h^2 P_c}{12\eta L} = \frac{\sigma h \cos\theta}{6\eta L} \longrightarrow L = \sqrt{\frac{\sigma h \cos\theta}{3\eta} t} \qquad \text{(2D)}, \tag{1.3a}$$

$$\dot{L} = \frac{r^2 P_c}{8\eta L} = \frac{\sigma r \cos\theta}{4\eta L} \longrightarrow L = \sqrt{\frac{\sigma r \cos\theta}{2\eta} t} \qquad \text{(3D)}, \tag{1.3b}$$

where η is the dynamic viscosity of the wicking liquid and t stands for time. This solution does not include the inertia, and the initial velocity at $t = 0$ is infinite, and it fails to describe the initial stages of wicking adequately. This simplification has caused problems in many applications, usually when gravity is present [40]. Nevertheless, it works well for long slender capillaries, networks of small pores, or densely-packed fine granular media, where the effects of inertia are minimal. However, it has also been shown that it is not an acceptable model for various fibrous materials due to the omission of inertia [41].

1.5 Bosanquet's Theory

Shortly after Washburn's work, Bosanquet introduced an ODE to describe the dynamics of the capillary rise, taking inertia into account for the first time [42]. Bosanquet equation for both flat channels (2D) and tubes (3D) are given below, respectively,

$$\rho\left(L\ddot{L} + \dot{L}^2\right) + \frac{12\eta}{h^2} L\dot{L} + \rho g L = \frac{2\sigma}{h}\cos(\theta) \qquad \text{(2D)}, \tag{1.4a}$$

$$\rho\left(L\ddot{L} + \dot{L}^2\right) + \frac{8\,\eta}{r^2}\, L\dot{L} + \rho g L = \frac{2\sigma}{r}\cos(\theta) \qquad \text{(3D)}, \tag{1.4b}$$

with ρ being the mass density of the wicking liquid. The first term ($\rho\left(L\ddot{L} + \dot{L}^2\right)$) constitutes the effect of inertia in the process of capillary rise and distinguishes Bosanquet's equation from Washburn's (Equation 1.3). Various works have investigated different regimes during the capillary rise. Traditionally, alongside the ubiquitous Reynolds number (Re, the ratio of the inertial to the viscous forces), two other non-dimensional numbers describe the regime transition in capillary flows, Ohnesorge number (Oh, the ratio of the viscous to the inertial and surface tension forces) and Bond number

(Bo, the ratio of gravitational to surface tension forces). These thresholds of regime transition are roughly demarcated by the capillary and viscous time scales (t_c and t_v, respectively) in the literature [43, 44]. Table 1.1 defines these values for both flat channels (2D) and tubes (3D, axisymmetric), respectively.

Table 1.1: Some frequently used non-dimensional numbers (Reynolds (Re), Ohnesorge (Oh), and Bond or Eötvös (Bo) numbers) in relevant capillarity problems together with the viscous (t_v) and capillary (t_c) time scales. The viscous time scale and Oh/Bo ratio are traditionally associated with regime transition in capillary flows in the literature, represented for a flow between parallel sheets (2D) [45] and in a simple tube (3D) [43] with the hydraulic radii of h and r, respectively.

Geometry	Re	Oh	Bo	t_c	t_v
Channel (2D)	$\overline{u}h/\nu$	$\eta/\sqrt{2\rho\sigma h}$	$\rho g h^2/\sigma$	$\sqrt{\rho h^3/\sigma}$	h^2/ν
Tubular (3D)	$2\overline{u}r/\nu$	$\eta/\sqrt{2\rho\sigma r}$	$\rho g r^2/\sigma$	$\sqrt{\rho r^3/\sigma}$	r^2/ν

The dominant force during the capillary rise changes over time, from a purely inertial or *inviscid* regime (Quéré's linear law, $L \propto t$ [40]) to a visco-inertial regime (Bosanquet's solution), then when inertial effects become insignificant, to purely viscous (diffusive, Washburn's law, $L \propto \sqrt{t}$), and –if gravity is present– eventually to a visco-gravitational regime that leads to a stand at Jurin's height if Oh/Bo $\ll 1$, meaning that viscous forces are not strong enough to stop the meniscus upon reaching Jurin's height [44, 46]. Although some earlier studies [40, 43, 45] have also proposed an initial $L \propto t^2$ regime prior to Quéré's linear law to fulfill the velocity continuity at $t = 0$, Das *et al.* later stated that this regime could essentially be any power law in the form of $L \propto t^n$ (where $n > 1$) and not necessarily $n = 2$ [47]. Fries *et al.* described these regime transition times in terms of the viscous time scale (t_v) [46].

1.6 Irregular Capillaries

To this point, all the capillaries discussed were regular capillaries which only constitute canonical geometries of either uniform circular or very long rectangular (2D) cross-sections. Although these models are vastly used for many applications, they fail to accurately describe many other. Irregular

capillaries can be classified into two groups, the ones with varying circular or rectangular cross-sections (where the width of a channel or the radius of the tube is not constant) and capillaries with a constant but nontrivial cross-section (e.g., elliptical tubes [48]).

A special kind of irregular capillary, also known as Taylor rising, is the wicking of the liquid within the narrow wedge-shaped space between to angled surfaces and has been found to follow a universal $L \propto t^{1/3}$ law for the temporal evolution of the wetting front along the corner [49–51]. Moreover, when deformable capillaries are at play, the geometry undergoes *time-dependent* irregularities due to the *elastocapillary coalescence*, a more complicated phenomenon that occurs due to the interaction of the surface tension of the interface with deformable walls. Elastocapillary coalescence of parallel flexible sheets [52–54] and supple rods (such as strands of hair [55]) are typical examples. An extensive review of elastocapillarity applications was presented by Bico *et al.* [56]. In this study, we only focus on the capillary flow in channels or tubes with varying width or radius and rigid, stationary walls.

Although Washburn's equation was developed for a simple geometry (originally a tube, later also derived for a channel with a 2D simplification [39]), it can be extended to describe wicking in irregular capillaries with axial variations (hereafter corrugation) through the geometrical extension of Hagen-Poiseuille equation [39]. The Hagen-Poiseuille equation relates the geometrical and physical properties of the flow with the viscous pressure drop, as presented below for flows between parallel plates (2D) and in tubes (3D),

$$Q = \frac{bh^2}{8\eta}\frac{\partial P}{\partial s}\int_{-h/2}^{h/2}\left[1 - 4\left(\frac{z}{h}\right)^2\right]\mathrm{d}z = \frac{bh^3}{12\eta}\frac{\partial P}{\partial s} \qquad \text{(2D)}, \tag{1.5a}$$

$$Q = \frac{\pi r^2}{2\eta}\frac{\partial P}{\partial s}\int_{0}^{r} R\left[1 - \left(\frac{R}{r}\right)^2\right]\mathrm{d}R = \frac{\pi r^4}{8\eta}\frac{\partial P}{\partial s} \qquad \text{(3D)}, \tag{1.5b}$$

where $Q = \iint_A u\, dA$ is the volumetric flow, h and b are the width and depth (or breadth) of a channel and r is the radius of a tube, with η representing the dynamic viscosity of the fluid. Knowing that $Q = bh(L)\dot{L}$ in a 2D and $Q = \pi r^2(L)\dot{L}$ in a tubular (3D) geometry, the viscous pressure drop can be found in irregular ducts (i.e., varying cross section, $h = h(s)$ and $r = r(s)$) by integrating $\frac{\partial P}{\partial s}$ from Equation 1.5 over the wicking length ($0 < s < L$) for both geometries,

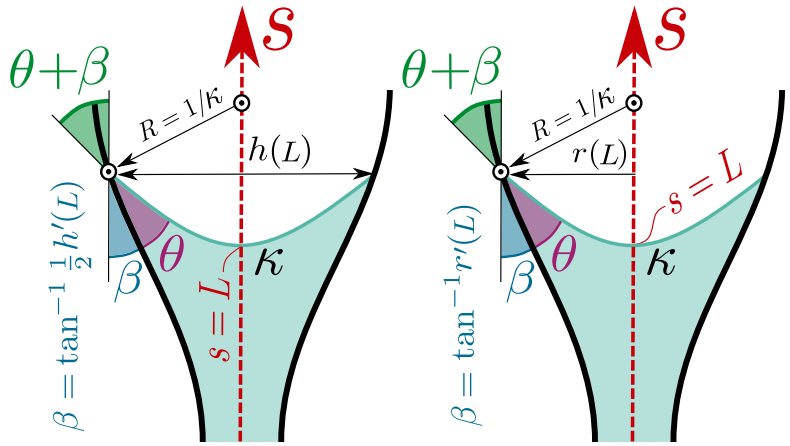

(a) Channel (2D) (b) Tube (3D)

Figure 1.2: Geometric dependence of the meniscus configuration on the wall angle (β) and (a) the width of a channel ($h(s)$) and (b) the radius of the tube ($r(s)$) at the meniscus ($s = L$). θ is the contact angle of liquid-gas interface with the solid wall ($0 \leq \theta \leq \pi/2$), $R = 1/\kappa$ is the radius of the meniscus (κ being the curvature of the meniscus), $h(s)$ is the width of the channel normal to its centerline and $r(s)$ is the radius of a tube to its axis, and s is the arc length coordinate of the centerline of the channel. For small wall angles, the approximation of $\beta \approx \tan\beta$ may be applied but not necessarily required.

$$P_v = -12\eta h(L)\dot{L} \int_0^L \frac{\mathrm{d}s}{h^3(s)} \qquad \text{(2D)}, \tag{1.6a}$$

$$P_v = -8\eta r^2(L)\dot{L} \int_0^L \frac{\mathrm{d}s}{r^4(s)} \qquad \text{(3D)}. \tag{1.6b}$$

The irregular capillary channels and tubes investigated in the literature are predominantly only corrugated and not tortuous [39, 57], However, a single tortuous (but not corrugated) capillary tube is investigated in [58]. *Tortuosity* (τ) is a global property of a curve (as opposed to curvature, which is a local property) that can be attributed to the axis or the centerline of capillary tubes or channels. It is defined as the ratio of the arc length of a curve to its end-to-end distance ($\tau \geq 1$). Tortuosity and curvature are related geometrical properties [59]. The effects of tortuosity on the diffusion of the porous media have also been studied in [60–62]. A schematic view

of irregular channels and tubes is shown in Figure 1.2. The analysis of irregular capillaries requires accounting for the rotation of the tangent to the walls (angle $\beta = \tan^{-1} \frac{1}{2} h'(L)$ for a channel and $\beta = \tan^{-1} r'(L)$ for a tube, as shown in Figure 1.2(a) and (b), respectively), which results in the fluctuations of the meniscus curvature since the contact angle is now modified to be $\theta + \beta$. Consequently, the capillary pressure (Equation 1.1) changes at every point in the capillary in clear contrast to flat geometries where the shape of the meniscus and capillary pressure is preserved through the rise; except during the very first moment of interface contact and gravitational oscillations. The rate of the rise for a *symmetric*, irregular channel (2D) or tube (3D) is given as,

$$\dot{L} = \frac{2\sigma \cos\left(\theta + \beta(L)\right) - \rho g L h(L)}{12\eta h^2(L) \int_0^L \frac{\mathrm{d}x}{h(x)^3}} \qquad \text{(2D)}, \tag{1.7a}$$

$$\dot{L} = \frac{2\sigma \cos\left(\theta + \beta(L)\right) - \rho g L r(L)}{8\eta r^3(L) \int_0^L \frac{\mathrm{d}x}{r(x)^4}} \qquad \text{(3D)}. \tag{1.7b}$$

Equation 1.7 (hereinafter extended Washburn's equation) has been used to study many applications of symmetric geometries, such as converging-diverging stepped-wall [63, 64], sinusoidal [57], conical (V-shaped) and power-law diverging tubes [39]. An important conclusion is that periodic deviations from a flat geometry that keep the average width or radius constant always hinder the wicking [65]. However, if no such constraint is applied, optimal profiles may be proposed to beat Washburn's square-root law [66, 67]. Alike Washburn equation (Equation 1.3), the extended Washburn equation given in Equation 1.7 suffers from an asymptotic singularity at $t = 0$ where inertial effects dominate the capillarity rise.

1.7 Numerical Simulation of Capillarity

Various numerical methodologies were employed in the literature to evaluate the validity of the theories of capillary filling, especially in intricate capillarity geometries. Arbitrary Lagrangian-Eulerian (ALE) [68], volume of fluid (VOF) [69], interface tracking [70], and free-surface lattice-Boltzmann (FSLB) [71] are among the most prominent methods. However, due to the rapid change of dominant forces from inertial to viscous to capillarity, these methodologies' spatial and temporal resolution has to be extremely refined.

This small resolution, in turn, increases the computational cost of the simulations, which limits the extent of the applicability of numerical solutions to specific geometries. Additionally, to properly describe the capillarity rise and interfaces, the spatial resolution in the numerical methods has to be discretized to levels much smaller than the capillarity high in equilibrium (i.e., L_J). This issue makes the generation of adequate discretization for the solutions of the equations laborious and time-consuming.

In that sense, developing governing equations to describe the different regimes in capillarity rise in channels and tubes with arbitrary geometries can be beneficial to understand and design engineering devices in many fields. However, to the best of our knowledge, a visco-inertial model that describes wicking in geometrically irregular capillaries with both tortuosity (curved centerline or axis) and corrugation (width or radius variation) is not available in the literature. Although Lei *et al.* proposed a solution for only corrugated tubes that including inertia, their solution does not consider the force exerted by the capillary wall in the force balance, thereby failing to satisfy the Young-Laplace equation at the meniscus [72]. Their solution critically fails to confirm with the existing literature when the inertial terms are omitted (i.e., the extended Washburn equation, Equation 1.7), resulting from the negligence of the force exerted by the wall in the force balance, thereby failing to satisfy the Young-Laplace equation at the meniscus [72].

1.8 Thesis Outline

This thesis intends to introduce a procedure to analyze irregular capillary channels (2D) and tubes (3D) with both corrugation and tortuosity, considering the inertial, viscous, and gravity effects. To do so, we propose a geometrical extension to Bosanquet's equation in irregular channels and tubes, accounting for the effects of the dynamic contact angle (DCA). We shall discuss further why the inclusion of inertia in the analysis of irregular capillaries and deriving a geometrical generalization of the Bosanquet equation is much more crucial compared to regular capillaries, and is the only means of investigations into the complexities regarding non-linear dynamics and multiple equilibria involved in capillarity in complicated geometries.

The remainder of this thesis is organized as follows,

Chapter 2 defines the problem of irregular capillaries, expresses the assumptions required to develop the theory of capillarity in complicated geometries, demarcates the limits of theory, and proposes a correction to the traditional Hagen–Poiseuille equation.

Chapter 3 is a detailed analysis of the problem. Implementing the Reynolds transport theorem on a generic volume element which eventually culminates in an integro-differential equation, governing the wikcing in irregular capillaries.

Chapter 4 presents the results from the derived ODE in Chapter 3 for some typical cases and compares them against their numerical and experimental counterparts from the literature and VOF simulations specifically conducted for this purpose. The effects of gravity and inertia on regime transition and Jurin's height are enlarged upon.

Chapter 5 will go over the concluding remarks as well as possible future work recommendations.

Chapter 2

Problem Statement

To obtain the governing equation on the position of the meniscus or the wicking length (L) in a general geometry for an inertial observer, the Young-Laplace equation (Equation 1.1) must be satisfied at all times at the meniscus which is the principal governing law of capillary phenomena. However, to be able to derive a formulation for capillarity through the laws of continuum mechanics, a set of simplifications and demarcations deems crucial, which are to be discussed in this chapter.

It is assumed that the meniscus always preserves its circular cross-section except at the very early stages of the rise where it transitions from flat to circular in a very short time scale. In this regard, the radius of a tubular capillary (r) or the half-width of a channel ($h/2$) must be smaller than the capillary length $\lambda_c = \sqrt{\sigma/\rho g}$, which is the ultimate length scale for the surface tension to sustain a curved meniscus. The meniscus is considered not to undergo distortions, surface waves, or rupture (during bubble or droplet formation) due to inertial effects [73]. Any possible effects of gravity on the configuration of the meniscus in inclined or tortuous capillaries is neglected. Such effects are especially discussed and investigated in [74].

The wicking liquid is incompressible (at constant density, i.e., $\frac{\partial \rho}{\partial t} = 0$ and $\nabla \rho = 0$, independently). It is assumed that the flow within the capillary is laminar and fully developed. Laminarity of the capillary flow is a pretty safe assumption and the maximum Re observed in our simulated cases never exceeded ≈ 300, which is much below the transition Re threshold to the turbulence, i.e., Re ≈ 1500 for a channel (2D) and Re ≈ 2000 for a tube (3D) [75]. To achieve a fully-developed flow, the capillarity has to have enough entrance length (immersed below the free surface of the reservoir, Figure 3.1). The effect of the entrance length and developing flow in capillarity was theorized in [76] and later verified against experiments in [43].

Laminarity and fully-developed flow dictate a parabolic velocity distribution across the capillary. This assumption is valid as long as the tortuosity

or corrugation of the capillary does not induce secondary flows and vortices. Dean's number (De) is traditionally used to assess the significance of secondary flows owing to the centripetal acceleration in tortuous ducts [77]. An adverse pressure gradient is generated owing to the curvatures in the channel, which drives secondary (non-trivial) flows that are superimposed on the primary (trivial) flow. Another issue rises in the initial stages of capillary rise, when an inertial regime of fluid flow is dominant. The assumption of the parabolic velocity distribution requires a non-inertial flow, nonetheless, we have assumed the velocity profile is parabolic even in the inertial regime. A more rigorous investigation of this assumption requires an asymptotic analysis of the inertial terms.
Dean number is described as $\mathrm{De} = \mathrm{Re}\sqrt{\kappa_{\mathrm{cen.}} D_h}$, where $D_h = 4A/p$ is the hydraulic diameter of the duct (with A and p being the cross-sectional area and wet perimeter, respectively) and $\kappa_{\mathrm{cen.}}$ represents the curvature of the duct's either centerline (2D) or axis (3D).

For planar curves such as the centerline of a channel ($c(x)$ in Figure 2.1(a)), the curvature is calculated as $\kappa_{\mathrm{cen.}} = |c''|/(1 + c'^2)^{3/2}$, where $c'(x) = \frac{\mathrm{d}c}{\mathrm{d}x}$ and $c''(x) = \frac{\mathrm{d}^2c}{\mathrm{d}x^2}$. For a tube, the hydraulic diameter is simply its diameter, and for rectangular duct $D_h = 2h^s b/(h^s + b)$. Since in a nearly 2D geometry $h \ll b$, the hydraulic diameter is $D_h \approx 2h$. Dean's number is represented for both geometries below,

$$\mathrm{De} = \mathrm{Re}\sqrt{2\,h\,\kappa_{\mathrm{cen.}}} \qquad (2D), \tag{2.1a}$$

$$\mathrm{De} = \mathrm{Re}\sqrt{2\,r\,\kappa_{\mathrm{cen.}}} \qquad (3D). \tag{2.1b}$$

When Dean's number is below 40, the flow can be assumed to be unidirectional [78]. At $\mathrm{De} \approx 64$ the secondary flows begin to manifest in mushroom-shaped patterns [78]. Therefore, our theory is also valid for $\mathrm{De} < 40 - 60$.

2.1 Rectification of Tortuous Channels and Tubes

The analysis of the tortuous ducts requires taking the rotation of the meniscus into account. We assume the rotation of the meniscus is around the centerline of a channel (2D) or the axis of a tube (3D). A channel or tube is symmetric with respect to its true centerline or axis, respectively. We adopt an approach in which we straighten the centerline and turn the hitherto-tortuous channel into a longer, non-tortuous channel. The new channel is

to be analyzed like a symmetric, corrugated channel onward under the conditions mentioned above.

We called this approach the *centerline rectification* which is schematically described in Figure 2.1. Although the theory applies to both channels and tubes, we explain the centerline determination and rectification process for channels and assume that a tortuous tube's axis and radius function is known.

2.1.1 Centerline Determination

Centerline rectification causes the normal width (h) to be different from the horizontal width ($h^x(x) = |h_l^x - h_r^x|$) in tortuous channels, as shown in Figure 2.1 (top-left panel). To find the centerline along which the rectification is to happen, one may assume under low tortuosity that the centerline may be approximated with the average of the wall functions, i.e., $c(x) = (h_l^x + h_r^x)/2$ (dashed line in Figure 2.1). The normal or rectified width may then be found through finding the wall function values at contact points with the meniscus, which is rotated at the angle $\alpha = \tan^{-1} c'(x)$ with respect to the x-axis,

$$h = \frac{1}{2}\sqrt{c'^2(x) + 4}\Big[h_l^x(x - \delta) - h_r^x(x + \delta)\Big], \tag{2.2}$$

where $\delta = c'(x)|h_l^x - h_r^x|/2$.

2.1.2 Voronoi Segmentation

The centerline obtained through the average of the wall functions is not the true centerline when the channel is not symmetric, i.e., the centerline itself is tortuous. The discrepancy grows larger as the curvature of the centerline increases. The true centerline is the one whose normal is intercepted by both wall functions at the same distance, posing it at the center of the orthogonal transect at each point.

To find the true centerline that satisfies this condition at all points, we shall resort to the Voronoi segmentation scheme. This method, alongside its other variant, the Delaunay triangulation, has been widely used in the determination of the width of rivers, a crucial parameter in the analysis of their morphological evolution [79].

We have adopted the Voronoi segmentation scheme and filtering procedure described by A. Golly and J. M. Turowski to determine the true centerline [80]. The discrepancy between the true (Voronoi-obtained) and average centerlines are depicted in Figure 2.2 for four sinusoidal channels at different phase shifts. The only channel in which both centerlines exactly match is the symmetric channel, where $\psi = \pi$ (not shown).

After finding the true centerline, the normal width of the channel (h) at any point on the arc-length coordinate (s) may be calculated as the wall-to-wall length of the orthogonal transect at the point in question.

Now all relations applied on non-tortuous, corrugated channels can be reformulated in terms of the arc length coordinates (s) and the normal width of the channel (h), obtained by either Equation 2.2 for relatively low tortuosities or Voronoi segmentation scheme for a more accurate analysis. However, aside from the tortuosity, the corrugation challenges the assumption of the unidirectional flow either, and the extend of such effect must be investigated. Although the Hagen-Poieseuille equation may be extended to corrugated geometries (Equation 1.5), the validity of this relation is to be put to examination in the following section.

2.2 Correction of the Hagen–Poiseuille Equation in Corrugated Channels

The geometrically extended Hagen–Poiseuille equation (Equation 1.5) is only valid at low Reynolds numbers and for very small wall deviations where the *lubrication approximation* holds, so that it can be assumed that the flow is unidirectional [66]. Consequently, the theory fails to accurately evaluate the pressure drop at either higher Reynolds numbers or considerable corrugations of a duct. It underestimates the viscous shearing stress on the walls resulting from neglecting other components of the velocity field normal the primary flow direction. Thus, correction to the viscous pressure drop (Equation 3.15) is required in such conditions.

To investigate the discrepancy between the Hagen–Poiseuille and 2D Navier–Stokes (solved with CFD) flow rate predictions, we exposed over 600 symmetric sinusoidal channels with geometries of different widths (h_0), amplitudes (a), and wavelengths (λ) to a constant end-to-end average pressure

gradient ($\Delta P/L$) and compared the induced volumetric flow rate predicted by Hagen–Poiseuille ($\mathrm{Q_{H-P}}$) with that of the CFD simulation ($\mathrm{Q_{CFD}}$). It was observed that always $\mathrm{Q_{CFD}} \leq \mathrm{Q_{H-P}}$, i.e., $\mathrm{Q_{CFD}}/\mathrm{Q_{H-P}} \leq 1$. This ratio was very close to one for almost flat channels and relatively low Reynolds numbers and decreased as the channel became more corrugated, or the Reynolds number increased.

Multiple correlations combining the Reynolds number and the key geometric parameters in corrugation (i.e., h_0, a, and λ) were tried to show the functionality. The only satisfactory correlation came out of a novel dimensionless number for corrugated channels, ζ, similar to Dean number for tortuous ducts, defined as,

$$\zeta = \varepsilon \mathrm{Re} = \mathrm{Re}\sqrt{ah}/\lambda, \tag{2.3}$$

where $\varepsilon = \sqrt{ah}/\lambda$ is the dimensionless corrugation number. We now defined a viscous correction factor as the ratio of the CFD to Hagen-Poiseuille predicted flow rates $\xi = \mathrm{Q_{CFD}}/\mathrm{Q_{H-P}}$ which is plotted against ζ in Figure 2.3. A homographic trend line of $(1 + 0.085\,\zeta)^{-1}$ may also be used to approximately evaluate the ξ. In this study, the viscous correction factor was evaluated only for channels (2D), as the cases we investigated in this paper were only channel (2D) geometries. However, a similar viscous correction factor may also be obtained for tubes (3D).

To modify the theoretical flow rate in corrugated channels obtained by the Hagen-Poiseuille equation, the viscous pressure drop (Equation 1.6a) needs to be increased by a factor of $1/\xi$ so that the induced flow rate is inversely decreased,

$$P_v = -\frac{1}{\xi} 12\eta h(L)\dot{L} \int_0^L \frac{\mathrm{d}s}{h^3(s)} \qquad \text{(2D)}. \tag{2.4}$$

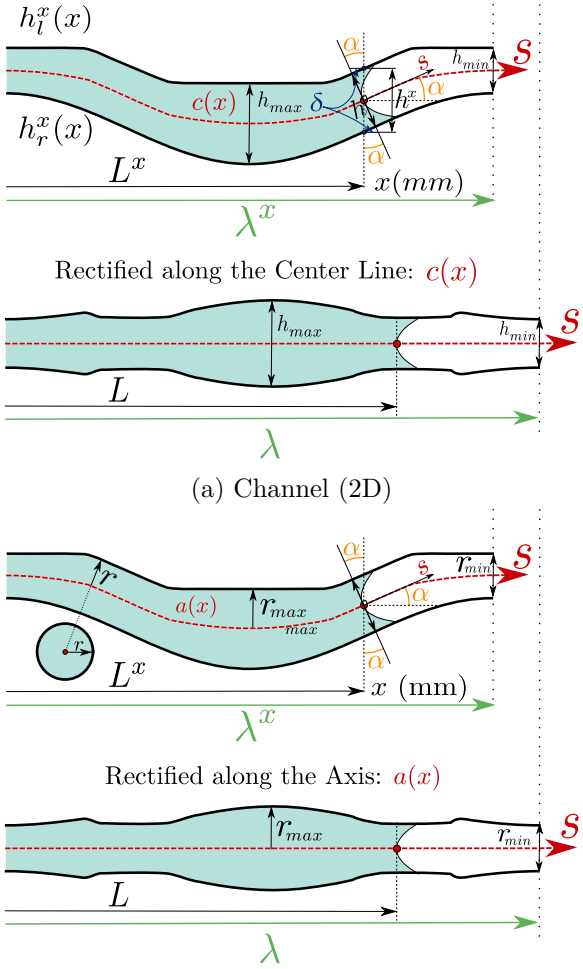

(a) Channel (2D)

(b) Tubular (3D)

Figure 2.1: Schematic of the rectification process. In (a), above is the original tortuous periodic channel, and below the *rectified* channel is presented within a single wall wavelengt, while (b) shows a tube and its rectified counterpart. $h_l^x(x)$ and $h_r^x(x)$ are the functions describing the left and right walls of the original channel, respectively; and $c(x)$ is the centerline function $c(x) = (h_l^x + h_r^x)/2$ and the horizontal (unrectified) width is defined as $h^x(x) = |h_l^x - h_r^x|$. The original wall wavelength is λ^x, while it is increased to λ after rectification ($\lambda^x \leq \lambda$). L^x is the height to which the liquid has risen, while L denotes the wicking length ($L^x \leq L$). α is the angle of meniscus rotation ($\cos\alpha(s) = \hat{\mathbf{e}}_x \cdot \hat{\mathbf{e}}_s$). For tortuous tubes, it is assumed that the axis and the normal radius are prescribed.

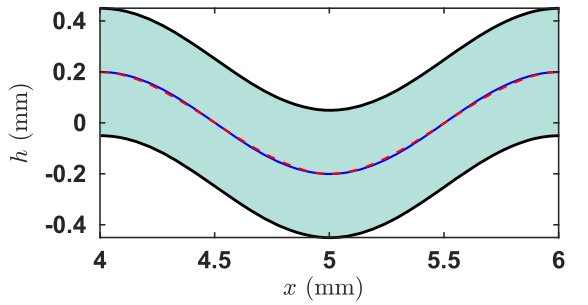

(a) $\psi = 0$

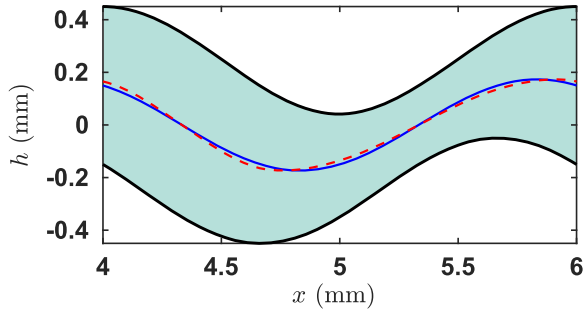

(b) $\psi = \pi/3$

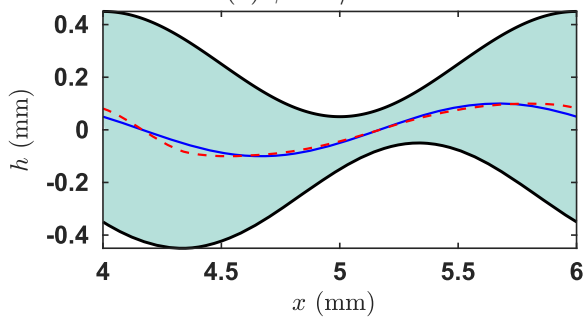

(c) $\psi = 2\pi/3$

Figure 2.2: The comparison of the average (continuous blue) and Voronoi (dashed red) centerlines in for types of sinusoidal channels, (a) anti-symmetric ($\psi = 0$), (b) shifted at $\psi = \pi/3$, (c) shifted at $\psi = 2\pi/3$. Note that the two centerlines coincide at $\psi = \pi$ phase shift, i.e., a symmetric (non-tortuous) channel. Other geometric parameters constitute $h_0^x = 0.5$ mm, $a^x = 0.2$ mm, and $\lambda^x = 2$ mm.

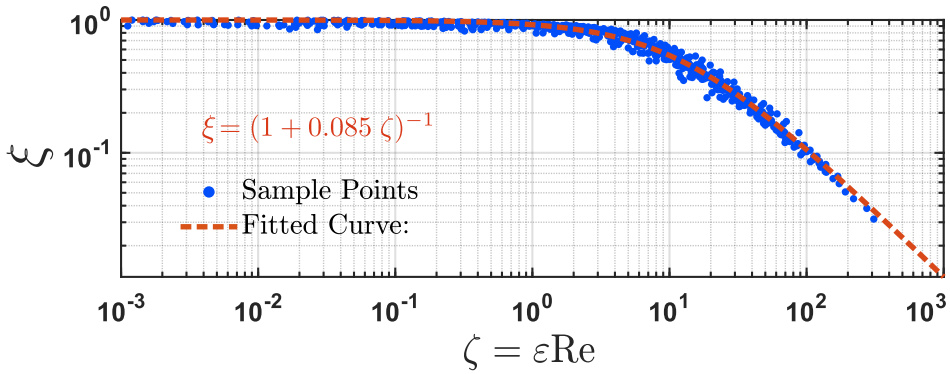

Figure 2.3: The viscous correction factor (ξ, the ratio of the CFD-obtained predicted volumetric flow rate to that of the Hagen–Poiseuille equation) is plotted against the newly defined variable $\zeta = \varepsilon \mathrm{Re}$ in a bilogarithmic scale, which may also be estimated by a homographic trend line of $(1 + 0.085\,\zeta)^{-1}$.

Chapter 3

Analysis

We would like to derive the governing equation on the wicking length ($L(t)$) in irregular channels (2D) and tubes (3D). Figure 3.1 shows the schematics for an irregular channel with the most important geometrical features and forces. The geometrical features of the channel are shown in Figure 3.1(a), where the effect of the corrugation and tortuosity is shown in the undulations of the channel's walls. In order to perform the force balance, it is now convenient to take an arbitrary infinitesimal element in the capillarity, as shown in Figure 3.1(b).

It is interesting to see that in addition to the contact angle (θ) between the solid-fluid interface that drives capillarity rise in regular channels and tubes, an additional geometrical factor appears due to the corrugation and tortuosity of the channel or tube as denoted by the tangent angle β (see Figure 3.1(b)).

Next, we perform the balance of forces in the differential frustum-shaped volume element, as shown in Figure 3.1(c). Since the pressure force exerted by the capillary wall is not as trivial as in a simple capillary (in which the force from the wall equates the viscous friction force, as undertaken by Xiao *et al.* [81]), especially in tortuous capillaries, it is much reasonable to write the Reynolds transport theorem for a volume element, integrated over the cross-section, using an Eulerian analysis of the liquid.

3.1 Reynolds Transport Theorem

That mentioned, we need to write the conversation laws on a generic volume element. The Eulerian analysis of the fluid dictates volumetric flux at the inlet and outlet cross-sections of the element. To write the balance of forces for such volume, Reynolds Transport Theorem must be implemented which is essentially a representation of Leibniz rule integration of integration for a

deforming and moving control volume. We expand the left-hand side (the resultant force along the centerline or axis). A more basic form of the force balance is presented in Appendix A, which is then simplified to,

$$\mathrm{d}F_s = 2b\tau \mathrm{d}s \;-\; bh\,\frac{\partial P}{\partial s}\mathrm{d}s \;-\; \rho bhg_s \mathrm{d}s \quad \text{(2D)}, \tag{3.1a}$$

$$\mathrm{d}F_s = 2\pi r\tau \mathrm{d}s - \pi r^2 \frac{\partial P}{\partial s}\mathrm{d}s - \rho g_s \pi r^2 \mathrm{d}s \quad \text{(3D)}. \tag{3.1b}$$

The first term in Equation 3.1 ($2b\,\tau\,\mathrm{d}s$) represents the contribution of the viscous force made by the wall in the centerline direction. τ is the shearing stress exerted in the wall due to the changing velocity profile of the fluid in the centerline direction. This stress will be related to the velocity gradient via a Newtonian model in the sequel. The second and third terms on the right-hand side of Equation 3.1, represent the force made by changes in the pressure and due to the gravitational force, respectively. Remarkably, $g_s = g\cos\alpha(s)$ is the projection of the acceleration gravity vector in the direction of the centerline, and $\cos\alpha(s) = \hat{\mathbf{e}}_x \cdot\ \hat{\mathbf{e}}_s$.

Having made the force balance in the infinitesimal element, we now compute the rate of momentum change via the Reynolds transport theorem. Written for an infinitesimal element in the capillarity located at an arbitrary point (s) in which the fluid has a velocity in the inlet and outlet $u(s)$ and $u(s)+\frac{\partial u}{\partial s}$, respectively (see Figure 3.1(b)), is

$$\mathrm{d}F_s = \rho\frac{\partial}{\partial t}\Big[u(s)\mathrm{d}V\Big] + \rho\Big[\int_{A+\mathrm{d}A} u^2(s+\mathrm{d}s)\mathrm{d}A - \int_A u^2(s)\mathrm{d}A\Big]. \tag{3.2}$$

In order to deal with average velocities over the cross-sections rather than the velocity fields, knowing that the velocity field follows a parabolic distribution, a *square-velocity average coefficient* (ϕ) may be defined as,

$$\begin{aligned}\phi \;=\; & \frac{1}{b\,h(s)\,\bar{u}^2(s)}\times \\ & \int_{-h/2}^{h/2} \frac{9}{4}\,b\bar{u}^2(s)\left[1 - 8\left(\frac{\ell}{h}\right)^2 + 16\left(\frac{\ell}{h}\right)^4\right]\,\mathrm{d}\ell \quad = \frac{6}{5}, \quad \text{(2D)}\end{aligned} \tag{3.3a}$$

$$\begin{aligned}\phi \;=\; & \frac{1}{\pi\,r^2(s)\,\bar{u}^2(s)}\times \\ & \int_0^r \;8\pi\;\bar{u}^2(s)\;\left[1\;-\;2\left(\frac{R}{h}\right)^2\;+\;\left(\frac{R}{h}\right)^4\right]R\,\mathrm{d}R = \frac{4}{3}. \quad \text{(3D)}\end{aligned} \tag{3.3b}$$

By applying the square-velocity average coefficient to Equation 3.2 we can remove the integration and work with the average velocities ($\bar{u}$) from here onwards,

$$\mathrm{d}F_s = \rho \frac{\partial}{\partial t} \left[u(s)\ \mathrm{d}V\right] + \rho\,\phi\,[\bar{u}^2(s+\mathrm{d}s)(A+\mathrm{d}A) - \bar{u}^2(s)A]. \tag{3.4}$$

To obtain the rate of the momentum change within the element, we consider the most general case where differential elements can expand. This case is usually unnecessary for most elements but required for the last element adjacent to the meniscus ($s = L$). The momentum change in Equation 3.2 can be expanded as

$$\rho \frac{\partial}{\partial t}[u(s)\mathrm{d}V] = \rho \left(\dot{u}(s)dV + u(s)d\dot{V}\right). \tag{3.5}$$

Next, we relate the volume expansion rate of the elements ($\mathrm{d}\dot{V}$) to the stretch rate of the differential arc length element ($\dot{\mathrm{d}s}$) below, and will later explain how this must be dealt with,

$$\begin{aligned} \mathrm{d}\dot{V} &= \frac{\partial}{\partial t}\ b\,[h(s)\mathrm{d}s\ +\ \frac{1}{2}h'(s)\mathrm{d}s^2] \\ &\approx\ b\,h(s)\,\dot{\mathrm{d}s} \qquad\qquad (2\mathrm{D}), \end{aligned} \tag{3.6a}$$

$$\begin{aligned} \mathrm{d}\dot{V} &= \frac{\partial}{\partial t}\ \pi\,[r^2(s)\mathrm{d}s + rr'(s)\mathrm{d}s^2] \\ &\approx \pi r^2(s)\,\dot{\mathrm{d}s} \qquad\qquad (3\mathrm{D}). \end{aligned} \tag{3.6b}$$

Knowing that the velocity of the fluid at the meniscus equals the velocity of the meniscus itself, i.e., $u_x(L,t) = \cos\alpha(L)\dot{L}(t)$, we express the continuity condition as,

$$Q(t)\ =\ bh(L)\,\dot{L}(t)\ =\ b\,h(0)\,u(0)\ =\ bh(s)\bar{u}(s) \quad (2\mathrm{D}), \tag{3.7a}$$

$$Q(t)\ = \pi r^2(L\,)\dot{L}(t) = \pi r^2(0)\,\bar{u}(0) = \pi r^2(s)u(s) \quad (3\mathrm{D}), \tag{3.7b}$$

which states that the volumetric flow rate ($Q(t)$) remains constant at all sections and only varies with time. Using Equation 3.6 and the continuity condition (Equation 3.7) and plugging in into Equation 3.5, the right hand side of Equation 3.4 can be simplified into,

$$\mathrm{d}F_s = \rho\ \left[\dot{Q}\mathrm{d}s + Q\dot{\mathrm{d}s}\right] + \rho\,\phi\left[(u + \frac{\partial u}{\partial s}\mathrm{d}s)^2(A + A'(\mathrm{d}s) - u^2A\right], \tag{3.8}$$

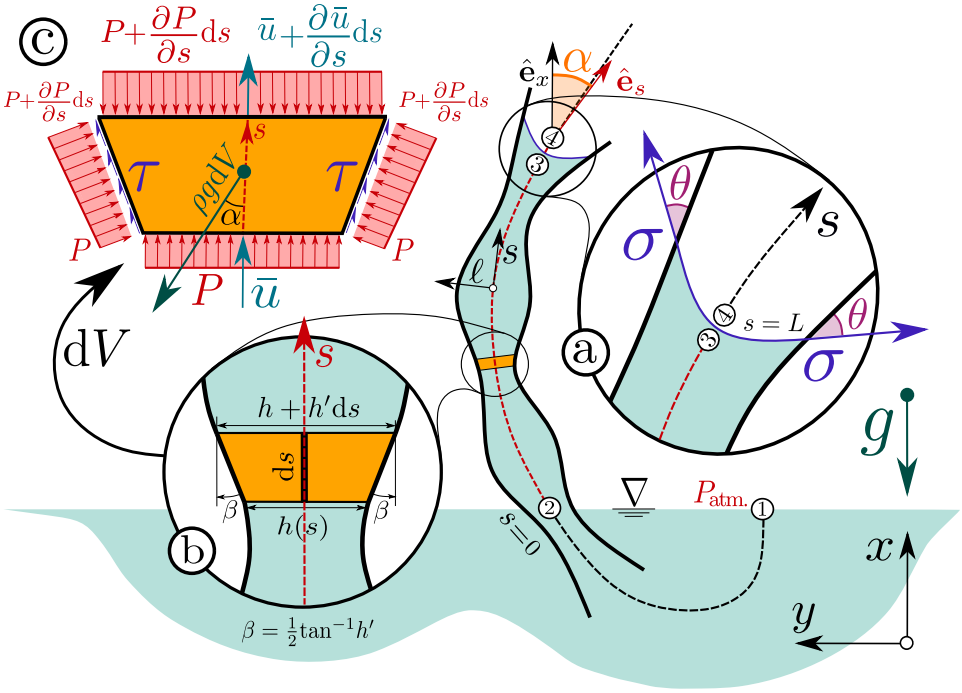

Figure 3.1: A schematic of the problem, a corrugated and tortuous channel (2D) is exposed to a liquid reservoir. (a) The meniscus moves across the centerline of the channel. A streamline beginning at the capillary mouth (point 2) and ending at the meniscus just behind the interface (point 3) is analyzed. The gravity is downward $\mathbf{g} = -g\ \hat{\mathbf{e}}_x$ and $\cos\alpha(s) = \hat{\mathbf{e}}_x \cdot \hat{\mathbf{e}}_s$, σ is the surface tension and θ is the liquid-solid contact angle. x and y are fixed spatial coordinated in the vertical and horizontal directions, respectively, while s and ℓ being tangent and normal to the centerline, respectively. (b) A generic volume element $\mathrm{d}V$ along a differential portion of the centerline ($\mathrm{d}s$) is also magnified with the corresponding dimensions (β being the wall angle with respect to the centerline and $h(s)$ is the normal, *rectified* width of the channel). Acting stresses (shearing τ and normal P, as pressure) and surface-averaged incoming and outgoing velocities ($\overline{u}$) are depicted in (c). The free surface at the atmospheric pressure ($P_{\mathrm{atm.}}$) is represented with a triple-underlined ∇ symbol. A tortuous tube (3D) amy also be investigated similarly, but not shown in this figure.

where $\dot{Q}$ being,

$$\dot{Q} = \quad b\,\dot{L}\,\frac{\mathrm{d}}{\mathrm{d}t}\,h(L) \;+\; bh(L)\,\ddot{L} \;=\; b\,h'(L)\,\dot{L}^2 \;+\; b\,h(L)\,\ddot{L} \quad \text{(2D)}, \tag{3.9a}$$

$$\dot{Q} = 2\pi r(L)\dot{L}\frac{\mathrm{d}}{\mathrm{d}t}r(L) + \pi r^2(L)\ddot{L} = 2\pi r'(L)\dot{L}^2 + \pi r^2(L)\ddot{L} \quad \text{(3D)}. \tag{3.9b}$$

With substituting $\dot{Q}$ from Equation 3.9 in Equation 3.8, and equating to Equation 3.1 we arrive at an expansion of the force balance the volume element along the centerline. By dividing both sides of the equation by the area of the section, i.e., $A(s) = bh(s)$ for a channel (2D) or $A(s) = \pi r^2(s)$ for a tube (3D), a pressure balance expression is obtained. We want to emphasize the necessity of this step, especially in the analysis of tortuous channels. The differential force balance (Equation 3.1) cannot be integrated over a curved line such as the centerline of a tortuous channel in the hope of obtaining a global force formulation, as the force is a vector entity and changes direction. However, by normalizing the force over the cross-sectional area, the obtained pressure expression may be integrated over a curve, as it is a scalar entity. Now by integrating the expression along the wicking length ($0 < s < L$), for a 2D geometry, the equation takes the form of,

$$\underbrace{\rho\left[h'(L)\dot{L}^2 + h(L)\ddot{L}\right]\int_0^L \frac{\mathrm{d}s}{h(s)} + \rho h(L)\dot{L}\int_0^L \frac{\dot{\mathrm{d}}s}{h(s)} + \rho\phi h^2(L)\dot{L}^2\int_0^L \frac{h'(s)}{r^3(s)}\,\mathrm{d}s}_{\text{inertial terms}} +$$

$$\underbrace{2\rho\phi\int_0^L u\frac{\partial u}{\partial s}\,\mathrm{d}s}_{\text{flux term}} \;-\; \underbrace{\int_0^L \frac{2\tau(s)}{h(s)}\,\mathrm{d}s}_{\text{viscosity term}} \;+\; \underbrace{\int_0^L \frac{\partial P}{\partial s}\,\mathrm{d}s}_{\text{pressure term}} \;+\; \underbrace{\rho g\int_0^L \cos\alpha(s)\,\mathrm{d}s}_{\text{gravity term}} \;=\; 0, \tag{3.10}$$

and for a tubular (3D) geometry,

$$\underbrace{\rho r(L)\left[2r'(L)\dot{L}^2 + r(L)\ddot{L}\right]\int_0^L \frac{\mathrm{d}s}{r^2(s)} + \rho r^2(L)\dot{L}\int_0^L \frac{\dot{\mathrm{d}}s}{r^2(s)} + 2\rho\phi r^4(L)\dot{L}^2\int_0^L \frac{r'(s)}{r^5(s)}\,\mathrm{d}s}_{\text{inertial terms}} +$$

$$\underbrace{2\rho\phi\int_0^L u\frac{\partial u}{\partial s}\,\mathrm{d}s}_{\text{flux term}} - \underbrace{\int_0^L \frac{2\tau(s)}{r(s)}\,\mathrm{d}s}_{\text{viscosity term}} + \underbrace{\int_0^L \frac{\partial P}{\partial s}\,\mathrm{d}s}_{\text{pressure term}} + \underbrace{\rho g\int_0^L \cos\alpha(s)\,\mathrm{d}s}_{\text{gravity term}} = 0. \tag{3.11}$$

3.2 Expansion of the Terms

The inertial, flux, viscosity, and pressure terms still need to be expanded. In the following sections, we expand and explain each term so that a final, simplified governing equation is eventually obtained.

3.2.1 Moving Boundary Term

The differential arc-length element stretch rate ($\dot{\mathrm{d}}s$) is zero everywhere except for $s = L$, where $\dot{\mathrm{d}}s = \dot{L}$, hence the integrals containing this term as,

$$\int_0^L \frac{\dot{\mathrm{d}}s}{h(s)} = \frac{\dot{L}}{h(L)} \quad \text{(2D)}, \tag{3.12a}$$

$$\int_0^L \frac{\dot{\mathrm{d}}s}{r^2(s)} = \frac{\dot{L}}{r^2(L)} \quad \text{(3D)}. \tag{3.12b}$$

This approach is similar to Leibniz integral rule ($\frac{\partial}{\partial t}\int_0^L f(s)\,\mathrm{d}s = \dot{L}\,f(L) = \int_0^L f(s)\,\dot{\mathrm{d}}s$) and is responsible for differentiation with respect to varying integration limits. Neglecting this term results in the loss of the necessary nonlinear velocity term ($\dot{L}^2$) in flat channels or tubes (where $h'(s)$ or $r'(s)$ are respectively zero). A more detailed explanation of this term is presented in Appendix B.

The integrals containing $h'(s)$ or $r'(s)$ can be simplified using $h'(s)\,\mathrm{d}s = \mathrm{d}h$

or $r'(s)\ \mathrm{d}s = \ \mathrm{d}r$, and be written as,

$$\int_0^L \frac{h'(s)}{h^3(s)}\ \mathrm{d}s = \frac{1}{2}\left[\frac{1}{h^2(0)} - \frac{1}{h^2(L)}\right] \quad \text{(2D)}, \tag{3.13a}$$

$$\int_0^L \frac{r'(s)}{r^5(s)}\ \mathrm{d}s = \frac{1}{4}\left[\frac{1}{r^4(0)} - \frac{1}{r^4(L)}\right] \quad \text{(3D)}. \tag{3.13b}$$

3.2.2 Flux Term

The flux term is also calculated through part-to-part integration and applying the continuity equation (Equation 3.7),

$$2\rho \int_0^L u\frac{\partial u}{\partial s}\ \mathrm{d}s = \rho \dot{L}^2 \left[1 - \frac{h^2(L)}{h^2(0)}\right] \quad \text{(2D)}, \tag{3.14a}$$

$$2\rho \int_0^L u\frac{\partial u}{\partial s}\ \mathrm{d}s = \rho \dot{L}^2 \left[1 - \frac{r^4(L)}{r^4(0)}\right] \quad \text{(3D)}. \tag{3.14b}$$

3.2.3 Viscous Term

To obtain the viscous term, we need to derive the shearing stress for a laminar, *Newtonian fluid*. Since $\overline{u}$ is the average velocity over the cross section, the parabolic velocity distribution field (u) can be written for a 2D geometry as $u(s,\ell) = \frac{3}{2}\ \overline{u}(s)[1 - 4(\ell/h(s))^2]$, where ℓ is the normal coordinates to the arc length coordinate (s). Also, for a tubular (3D) geometry $u(s,R) = 2\ \overline{u}(s)[1 - (R/r(s))^2]$, where R is the radial variable normal to the arc length coordinate. Substituting the shearing stress on the walls adjusted by the viscous correction factor (ξ), i.e., $\tau = (\eta/\xi)\ \frac{\partial u}{\partial \ell}\ |_{\ell=h/2}$ (2D) and $\tau = (\eta/\xi)\ \frac{\partial u}{\partial R}\ |_{R=r}$ (3D) respectively in the viscous term of Equations 3.10 and 3.11, we obtain,

$$P_v = \int_0^L \frac{2\tau(s)}{h(s)}\ \mathrm{d}s = -\frac{12}{\xi}\,\eta h(L)\,\dot{L}\int_0^L \frac{\mathrm{d}}{h^3(s)} \quad \text{(2D)}, \tag{3.15a}$$

$$P_v = \int_0^L \frac{2\tau(s)}{r(s)}\ \mathrm{d}s = -\frac{8}{\xi}\,\eta r^2(L)\,\dot{L}\int_0^L \frac{\mathrm{d}}{r^4(s)} \quad \text{(3D)}, \tag{3.15b}$$

which yields the same results as the generalized Hagen–Poiseuille equation (Equation 1.6) when $\xi = 1$.

3.2.4 Pressure Term

The pressure term is equal to the pressure difference of the base of the capillary and the point just behind the meniscus, which are points 2 and 3 in Figure 3.1, respectively. Assuming a single streamline stretching from point 1 to point 2, one may deduce from Bernoulli's principle that an increase in the velocity of the liquid induces a dynamic pressure drop at the mouth of the capillary. However, this is not considered Bosanquet's assumptions, and including such a term will produce inconsistencies with the traditional Bosanquet equation (Equation 1.4) where no geometric irregularity exists. A similar approach to that of Fries and Dreyer's [46] based on Levine *et al.* solution for the pressure field at the entrance [76] may be adopted to consider such effect. However, this is beyond the scope of this study, for we aim at obtaining the geometrically extended version of the Bosanquet equation.

$$\int_0^L \frac{\partial P}{\partial s}\,\mathrm{d}s = [P_{\text{atm.}} - P_c] - [P_{\text{atm.}} - 0] = -P_c. \tag{3.16a}$$

The capillary pressure ($P_c = \sigma\kappa$) is dependent on the curvature of the meniscus. For regular capillaries, the curvature is constant. However, the curvature of the meniscus undergoes variations in irregular capillaries as the tangent to the wall changes direction (see Figure 1.2). The wall slope fluctuations change the curvature of the meniscus, leading to fluctuations in the capillary pressure (Equation 1.1). The implementation of the the dynamic contact angle is through an *exponential saturation* model $\cos\theta_{\text{dyn.}}(t) = \gamma(t)\cos\theta$, where $\gamma(t) = [1 - \exp(-\sigma t/\eta H)]$ as described in [81] for flat geometries. H is treated as an *ad hoc* constant in this study. For irregular capillaries, we discern that the exponential saturation term ($\gamma(t)$) of the DCA must be applied on the whole interface angle term ($\theta + \beta(L)$) and not merely the interface angle with the solid wall (θ). This condition is required as the interface must start from a flat state (zero capillary pressure) at $t = 0$ s regardless of the slope of the wall at that point ($L = 0$) and gradually transform into a meniscus. The capillary pressure for a corrugated channel (2D) or tube (3D) is then formulated as,

$$P_c = \gamma(t)\,\frac{2\sigma}{h(L)}\cos(\theta + \beta(L)) \quad \text{(2D)}, \tag{3.17a}$$

$$P_c = \gamma(t)\,\frac{2\sigma}{r(L)}\cos(\theta + \beta(L)) \quad \text{(3D)}, \tag{3.17b}$$

where $\beta = \tan^{-1} \frac{1}{2} h'(L)$ for a channel (2D) geometry and $\beta = \tan^{-1} r'(L)$ for a tubular (3D) geometry (cf. Figure 1.2(a) and Figure 1.2(b)). More details on the simulation and modeling of the dynamic contact angle are presented in Appendix C.

3.2.5 Gravity Term

The gravity term is identical for both geometries and is equal to the hydrostatic pressure (P_g),

$$\rho g \int_0^L \cos \alpha(s) \, \mathrm{d}s = \rho g L^x. \tag{3.18}$$

The gravity term is *path-independent* and is only a function of displacement in the gravity direction (L^x). Other body forces such as electromagnetism may also be treated similarly. Since $\cos \alpha(s)$ is only present in the gravity term, one may draw the important conclusion that the wicking length (L) will be independent of tortuosity or capillary inclination in the absence of gravity.

3.3 Governing ODE

This approach transforms Equations 3.10 and 3.11 into the Young-Laplace equation, which relates the pressure jump at the interface with the surface tension and the curvature of the interface as follows,

$$P_c \; = \; P_i + P_v + P_g \; = \; \sigma \kappa, \tag{3.19}$$

where P_c, P_i, P_v, and P_g are the capillary, inertial, viscous, and gravity (hydrostatic) pressure terms. To solve Equation 3.19 for the wicking length (L), we would like to reorder the expanded equation with respect to $\ddot{L}$, $\dot{L}^2$, $\dot{L}$, the surface tension and the gravity as,

$$\mathcal{A}(L) \, \ddot{L}(t) \; + \; \mathcal{B}(L) \, \dot{L}^2(t) \; + \; \mathcal{C}(L) \, \dot{L} \; + \; \mathcal{G}(L) \; = \; \mathcal{D}(L), \tag{3.20}$$

where $\mathcal{A}(L) \, \ddot{L}(t)$ and $\mathcal{B}(L) \, \dot{L}^2(t)$ are the inertial terms, $\mathcal{C}(L) \, \dot{L}$ is the viscous term, $\mathcal{G}(L)$ and $\mathcal{D}(L)$ represent the gravity and capillary (surface tension) terms, respectively. Equation 3.20 is an *integro-differential* equation whose

coefficients are given below for a channel (2D) geometry,

$$\begin{cases} \mathcal{A}_{2\mathrm{D}}(L) = \rho h(L) \displaystyle\int_0^L \frac{\mathrm{d}s}{h(s)}, & (3.21a) \\ \mathcal{B}_{2\mathrm{D}}(L) = \rho\Big[1 + h'(L) \displaystyle\int_0^L \frac{\mathrm{d}s}{h(s)} + \frac{3}{5}\left(1 - \frac{h^2(L)}{h^2(0)}\right)\Big], & (3.21b) \\ \mathcal{C}_{2\mathrm{D}}(L) = \dfrac{12}{\xi}\,\eta h(L) \displaystyle\int_0^L \frac{\mathrm{d}s}{h^3(s)}, & (3.21c) \\ \mathcal{D}_{2\mathrm{D}}(L) = \gamma(t)\,\dfrac{2\sigma}{h(L)}\cos\left(\theta + \beta(L)\right), & (3.21d) \\ \mathcal{G}_{2\mathrm{D}}(L) = \rho g \displaystyle\int_0^L \cos\alpha(s)\ \mathrm{d}s, & (3.21e) \end{cases}$$

and for a tubular (3D) geometry,

$$\begin{cases} \mathcal{A}_{3\mathrm{D}}(L) = \rho r^2(L) \displaystyle\int_0^L \frac{\mathrm{d}s}{r^2(s)}, & (3.22a) \\ \mathcal{B}_{3\mathrm{D}}(L) = \rho\Big[1 + 2r(L)r'(L) \displaystyle\int_0^L \frac{\mathrm{d}s}{r^2(s)} + \frac{2}{3}\left(1 - \frac{r^4(L)}{r^4(0)}\right)\Big], & (3.22b) \\ \mathcal{C}_{3\mathrm{D}}(L) = \dfrac{8}{\xi}\,\eta r^2(L) \displaystyle\int_0^L \frac{\mathrm{d}s}{r^4(s)}, & (3.22c) \\ \mathcal{D}_{3\mathrm{D}}(L) = \gamma(t)\,\dfrac{2\sigma}{r(L)}\cos\left(\theta + \beta(L)\right), & (3.22d) \\ \mathcal{G}_{3\mathrm{D}}(L) = \rho g \displaystyle\int_0^L \cos\alpha(s)\ \mathrm{d}s. & (3.22e) \end{cases}$$

This non-linear integro-differential equation (Equation 3.20) would be notoriously difficult to solve analytically. However, it can be solved numerically through linear interpolation of the non-linear integral functions given in Equations 3.21 and 3.22, thereby converting the non-linear integro-differential equation to a second-order non-linear ODE whose coefficients are known at any L. The obtained non-linear is then solved via Runge–Kutta algorithm.

The full-term equation represents the *extended Bosanquet equation* for irregular channels and tubes. Neglecting the inertial terms ($\mathcal{A}(L)\,\ddot{L}(t)$ and $\mathcal{B}(L)\,\dot{L}^2(t)$) yields the *extended Washburn equation* (Equation 1.7, but also

considering the effect of tortuosity or inclination). The equation is also simplified to an inclined symmetric capillary once α is constant ($\cos\alpha(s) = \cos\alpha$), conforming with the flat inclined tube studied in [82]. While removing the viscous term ($\mathcal{C}(L)\,\dot{L}$), leaves out all the dynamic terms and expresses the state of static equilibria when the gravity is present,

$$L_{J,i} = \frac{2\sigma\cos(\theta+\beta(L))}{\rho g h(L)} \qquad \text{(2D)}, \tag{3.23a}$$

$$L_{J,i} = \frac{2\sigma\cos(\theta+\beta(L))}{\rho g r(L)} \qquad \text{(3D)}, \tag{3.23b}$$

where $L_{J,i}$ is any possible solution for Jurin's height. We discuss later on that the Jurin's height ($L_J = \lim_{t\to\infty} L(t)$) is *path-dependent*, and the eventual state of static equilibrium can only be found through solving the full dynamic system for given initial conditions. Thus, contrary to simple geometries (Equation 1.2), no single static-equilibrium solution can necessarily be presented for irregular capillaries regardless of the conditions mentioned above. The numerical solution to the derived ODE is presented in the following section.

Chapter 4

Results and Discussions

4.1 Verification with Computational Fluid Dynamics

To evaluate the accuracy of our theoretical analysis, culminating in Equations 3.21 and 3.22, and to validate the numerical implementation of the non-linear integro-differential equation (Equation 3.20), we recourse to other numerical methods, cases from the literature, as well as experimental data.

To effectively simulate the capillary action within computational fluid dynamics simulations (CFD), both air and the wicking liquid are to be modeled and solved together, i.e., a multi-phase fluid simulation, to satisfy the Young-Laplace equation (Equation 1.1) on the free surface at the meniscus and to maintain the free surface of the reservoir at the atmospheric pressure ($P_{\text{atm.}}$). We have used Ansys® Academic Research Fluent, Release 19.2 Volume of Fluid (VOF) software to solve the Navier-Stokes equations for the multi-phase fluid simulations. As the VOF simulation are inherently multiphase, the air must be essentially simulated, with the properties of $\rho = 1.225$ kg.m^{-3} and $\eta = 1.79 \times 10^{-5}$ kg.m^{-1}.s^{-1}.

We used an explicit scheme for the VOF formulation in ANSYS fluent, coupled with a Level Set Method (LSM) for enhanced interface modeling. The body forces (such as gravity, if present in the problem) are included explicitly. A volume fraction cut-off threshold of 10^{-6} is used to demarcate the phases. The scaled resiudals must be monitored for the convergence of each step. Using a coupled solver, the convergence criteria (10^{-3} in our VOF simulations) must all be satisfied for each time step so that it is fully completed and the iterations are terminated. These criteria include continuity, $x-$velocity, $y-$velocity, volume fraction, and the level-set function. The convergence of the continuity is usually the hardest to achieve. The scaled residuals of the continuity equation normally start at 10^{-2} and end up 10^{-5} when the convergence criterion of 10^{-3} is met.

Apart from the criteria stated above, in order to obtain reliable results from numerical simulations, the following specific conditions were also followed:

4.1.1 Grid Independence and Meshing Considerations

a convergence criterion of 1% was used to determine the required general grid resolution. The spacing of the first layer of the grid also satisfied the $y^+ \leq 1$ condition to capture the boundary layer on the no-slip walls effectively. y^+ is a dimensionless value calculated as $y^+ = \sqrt{\tau_w \rho}/\eta$, where τ_w is the shear stress of the wall.

Furthermore, the three crucial geometrical cell shape parameters of *skewness*, *aspect ratio*, and *squish* were monitored so that the desirable accuracy is achieved [83]. A typical case of mesh convergence study is given in Appendix D.1.

4.1.2 Time Step Independence:

since the VOF simulations are inherently transient (time-dependent), the results must be independent of the temporal discretization. In this regard, the CFL[6] condition has been limited to 0.2, which is a safe threshold. For most cases, a fixed time step size of $\Delta t = 5 \times 10^{-6}$ s was deemed to be sufficient for this purpose. However, we discerned that sometimes smaller time steps were required due to meniscus perturbations, especially at narrow bottlenecks.

4.1.3 Domain Independence

to demarcate a finite domain of solution which is computationally reasonable, a number of artificial boundaries were required. These boundaries that define the outer borders of the solution domain might bring numerical artifacts to the solution. Hence, the boundaries were situated far enough from the region of interest, i.e., inside the capillary, so that the rise of the meniscus was not affected. We used a similar 1% convergence criterion as the outer boundaries were moved further to assess the convergence of the solution. Additionally, the liquid reservoir must be broad enough ($\sim$ 10 times as broad as the capillary itself) so that the height of the free surface does not considerably change owing to the wicking inside the capillary.

[6] Courant–Friedrichs–Lewy

Moreover, by constraining a contact angle of $\theta = 90^\circ$ on the outer surface of capillary walls (also with slip condition), there is no need for delimiters which are used in experimental and numerical studies to prevent meniscus formation outside of the duct [43, 84]. A detailed explanation of a domain convergence study is presented in Appendix D.2.

Figure 4.1(a) depicts several snapshots for a capillary rise within a symmetric sinusoidal channel modeled with VOF simulations. It can be seen from the figure that as time went by, the meniscus rose in the capillary. The red domain represents the liquid, while the blue domain represents air. Figure 4.1(b) shows the mesh inside the channel where wicking occurs. The structured mesh seamlessly transitions to higher refinement on the no-slip walls to satisfy the desired y^+ condition. Moreover, due to meniscus progression along the centerline, the mesh refinement must be higher than its perpendicular direction to capture the moving interface more effectively. Figure 4.1(c) shows the structured mesh within a tortuous channel and demonstrates the rotation of the mapped grid with respect to the tortuous centerline. Outside the capillary, a much bigger and irregular mesh was used for the air domain.

4.2 Validation of the VOF

Although the verification of the simulation is paramount, the results still need to be validated against experimental data to show that the simulations are, to some extent, the representation of reality. In this regard, we would like to benefit from the oft-cited published results of capillary rise in circular tubes under microgravity by Stange *et al.* [43]. In their study, they also investigated the effects of the dynamic pressure drop and the depth of immersion (L^*), none of which are included in our theoretical analysis but inherently included in the VOF simulations. In their investigation, Stange *et al.* [43], used silicone fluid (SF) as the wicking liquid with a surface tension of $\sigma = 0.0169$ N·m^{-1}, contact angle $\theta = 32.5^\circ$, viscosity $\eta = 0.818 \times 10^{-3}$ kg/m.s, and density $\rho = 818$ kg/m^3).

The comparison of the VOF results against those of Stange *et al.* is shown in Figure 4.2. Two simulations were performed with tube diameters of $d = 4$ mm and $d = 9$ mm using a different depth of immersion of $L^* = 10$ mm and $L^* = 50$ mm, respectively. The experimental data is shown with $\circ$ and $\triangle$ markers. The homologous simulations results are shown with solid lines.

We observed that the simulations results follow the experimental data closely with a maximum discrepancy less than 4% in both cases for the meniscus' height with time ($L(t)$). We also point out how the VOF simulations predict a zero slope at $t = 0$, which is in agreement with the trends of the experimental data. The discrepancy is thought to be at least in part due to a different dynamic contact angle theory used by Stange *et al.*, where $21^\circ \leq \theta_{\text{dyn.}} \leq 44^\circ$ [43]. To replicate the results, the equilibrium contact angle was discerned to be the average of this value in our simulations. The close agreement between the experiments and VOF simulations gave us confidence in our numerical set up, which we will use to assess the accuracy of the theory developed in Chapter 3.

The maximum discrepancy of the results of the height of the meniscus with time ($L(t)$) for the experiments and our VOF simulations is less than 4% in both cases. We may now deduce that the simulations are fairly accurate and can be used as the verification criterion for the theory developed in the previous section.

4.3 Results

To present the results, we investigate three 2D typical sinusoidal channels (anti-symmetric, shifted, and symmetric) at a lower and higher Reynolds ranges, totaling six cases. As the capillary rise is theoretically identical for all similar channels and wicking liquids, the Reynolds number is only a function of the geometry of the channel. In order to divide the cases into two categories of low and high Reynolds numbers, we assumed two sets of channels with the average distance between the walls of $h_0^x = 0.3$ mm and $h_0^x = 1.0$ mm at three phase shifts of $\psi = 0$ (anti-symmetric), $\psi = \pi/4$, and $\psi = \pi$ (symmetric). A more detailed specification of the geometry for each case and its corresponding non-dimensional numbers is presented in Table 4.1. The left and right wall functions of a generic sinusoidal channel (h_l^x and h_r^x) and its un-rectified width (h^x) are defined below,

$$h_l^x(x) = \quad h_0^x/2 \; + \; a^x \sin(2\pi \frac{x}{\lambda^x}), \tag{4.1a}$$

$$h_r^x(x) = -h_0^x/2 \; + \; a^x \sin(2\pi \frac{x}{\lambda^x} \; + \; \psi), \tag{4.1b}$$

$$h^x(x) = \quad h_l^x(x) \; - \; h_r^x(x). \tag{4.1c}$$

To assess each case through non-dimensional numbers, as per literature, the average of the maximum and minimum rectified widths of the channel ($\bar{h} = (h_{\max} + h_{\min})/2$) is designated as the characteristic length of a periodic corrugated channel [85].

Moreover, since the problems are transient, the velocity of the wicking liquid varies with time. One solution is to replace the wicking rate in the Reynolds number with a capillary characteristic velocity $v_c = \sqrt{2\sigma/\rho\bar{h}}$ [45]. However, the Reynolds number obtained this way represents a very short initial stage when the viscous forces are negligible, and the capillary and inertial forces predominantly govern the wicking, thereby yielding high Reynolds numbers (as high as ~ 300). Although we learn that even at the maximum velocity, the wicking is still below the turbulence threshold (~ 1500 for flows between parallel plates), it cannot be used in the assessment of the necessity and the evaluation of the viscous correction coefficient, as the wicking rate considerably drops after the viscous time scale (t_v). For the sake of consistency, the Reynolds number presented in Table 4.1 is calculated based on the temporal average of the wicking rate ($\dot{L}$) over the time span of $t_v < t < 2\,t_v$ to cover a period of visco-inertial capillary regime [46].

4.3.1 Lower Reynolds Results

Let us now focus on the results obtained for the channels with low Reynolds numbers ($\sim 30 - 40$ as detailed in Table 4.1). We notice that the three channels investigated (Cases 1−3) in this regime had Dean's number between $\sim 0 - 30$, and no viscous correction factor was used. Figure 4.3 shows the wicking length (L) *vs.* time and wicking rate ($\dot{L}$) *vs.* position in the channel for all three cases in Table 4.1. In Figure 4.3 results for VOF simulations (continuous lines), extended Washburn (dashed lines), extended Bosanquet (dotted lines), and extended Bosanquet with dynamic contact angle (DCA) (dot-dashed lines) are shown.

First, let us describe the results obtained with VOF for all simulations, as they will be used to assess the accuracy of the other approaches. It is evident from the meniscus position *vs.* time and the rate of meniscus rise with the position that the corrugations of the channels affected these quantities. Remarkably, the rise of the meniscus showed oscillatory values that corresponded with the geometrical fluctuations of the channels. See Table 4.1 for more details on the specifications of each case. Moreover, it is noteworthy to mention that although case 3 is purely corrugated, case 1 is not purely tortuous. A sinusoidal anti-symmetric channel does not have an exactly constant width, hence small fluctuations in its wicking rate (Figure 4.3(b)).

At the time $t = 0$ s, VOF simulations predicted a zero rise rate since inertial effects were considered when the Navier-Stokes equations were solved. This effect also manifested in the position of the meniscus *vs.* time, where the slope of the plots (Figure 4.3 left panels) is zero when $t = 0$ s.

Next, we focus our attention on the results obtained for the Ex. Bosanquet + DCA model. This model was the one closest to the VOF simulations, matching most of the characteristics of the solution. The Ex. Bosanquet + DCA solution matches well the VOF solution at $t = 0$ s in meniscus rise, and therefore, the meniscus position with time is accurately predicted (discrepancies are always less than $\sim 2\%$ for all cases). Next, the Ex. Bosanquet solution followed although the discrepancies grew compared to VOF.

In particular, the use of a constant contact angle increases the rate of rising of the meniscus, overestimating it over the first 2 mm of the capillary (see Figure 4.3 right panels). This effect was magnified at lower Reynold numbers and the discrepancy between VOF and Ex. Bosanquet increased as Re decreased. We finally discuss the results obtained with the for Ex. Washburn for Cases $1 - 3$. The solutions found with this approximation were the ones with the largest errors, which could grow up to $\sim 30\%$ on the meniscus position *vs.* time. This error is due to the singularity of the solution when $t = 0$ s since inertial effects are not considered. As discussed above, this issue manifests in an infinite wicking rate (see Figure 4.3 right panels), which tends to decrease with time. However, as can be seen in the figures, the differences in the wicking rate can extend for several undulations of the channels.

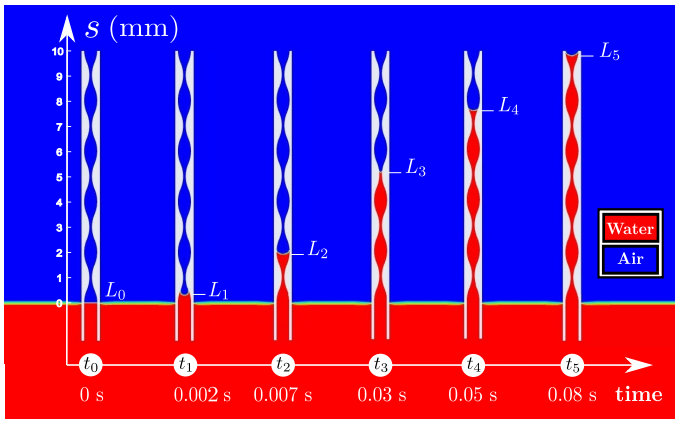

(a) Capillary rise in a typical symmetric sinusoidal channel simulated with VOF

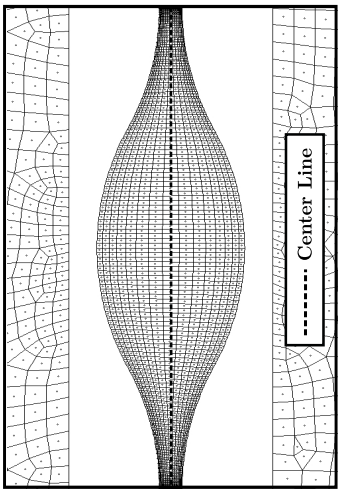

(b) Mesh configuration for a symmetric channel

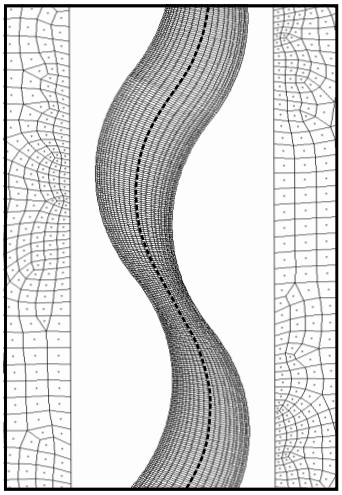

(c) Mesh configuration for a tortuous channel

Figure 4.1: The outlook of the VOF simulations, (a) shows multiple snapshots of the capillary rise in a sample case (Figure 4.3(c)) over time. Various configurations of the meniscus may be observed at different stages and wall angles. (b) demonstrates the spatial discretization of the domain through structured meshing in the same symmetric geometry, and (c) shows the structured mesh grid in a tortuous channel. The grid must rotate with the tortuous centerline to conform to the meniscus orientation best. Mesh resolution is relatively richer on the no-slip walls (internal surfaces of the channel) and at the bottlenecks to capture relatively higher field gradients.The outer surface of the tube is slippery and is assigned a $\theta = 90^\circ$ contact angle, thereby exerting no capillary rise outside of the capillary.

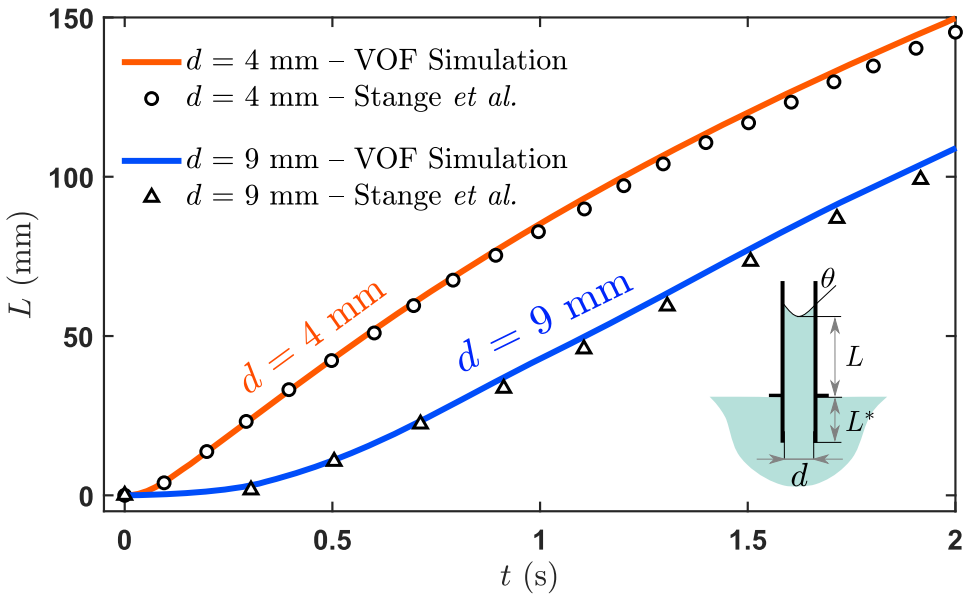

Figure 4.2: Comparing the VOF simulation results to the experimental data published by Stange *et al.* [43] The two cases constitute two cylindrical capillaries with different diameters (d) and depth of immersion (L^*), filled with a silicone fluid (SF 1.00) as the wicking liquid ($\sigma = 0.0169$ N·m^{-1}, $\theta = 32.5°$, $\eta = 0.818 \times 10^{-3}$ kg·m^{-1}·s^{-1}, and $\rho = 818$ kg·m^{-3}). (b) A snapshot from the contours of SF 1.00 volume fraction. The outer surface of the tube is slippery and is assigned a $\theta = 90°$ contact angle, thereby exerting no capillary rise outside of the capillary.

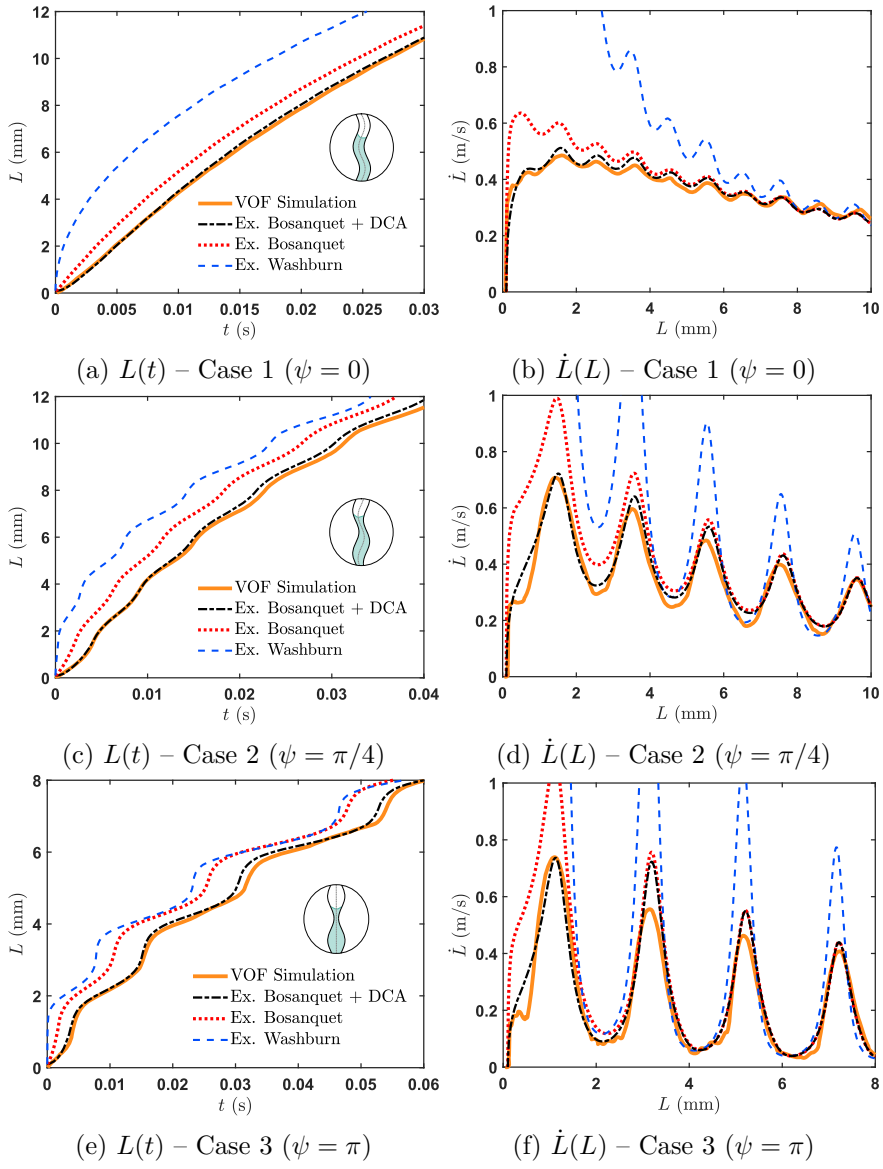

(a) $L(t)$ – Case 1 ($\psi = 0$)

(b) $\dot{L}(L)$ – Case 1 ($\psi = 0$)

(c) $L(t)$ – Case 2 ($\psi = \pi/4$)

(d) $\dot{L}(L)$ – Case 2 ($\psi = \pi/4$)

(e) $L(t)$ – Case 3 ($\psi = \pi$)

(f) $\dot{L}(L)$ – Case 3 ($\psi = \pi$)

Figure 4.3: Results of the wicking length variations with time ($L(t)$, left panels, (a),(c), and (e)) and the wicking rate with the meniscus position ($\dot{L}(L)$, right panels, (b),(d), and (f)) in lower Reynolds range ($\mathrm{Re} \sim 30 - 40$) for the extended Washburn (dashed blue lines), extended Bosanquet (with $\gamma(t) = 1$, dotted red lines), and extended Bosanquet + DCA (Equation 3.21, dot-dashed black lines) compared against VOF simulations (continuous orange lines) in three sinusoidal capillaries, (a) case 1, anti-symmetric ($\psi = 0$), (c) case 2, shifted at $\psi = \pi/4$, (e) case 3, symmetric ($\psi = \pi$).

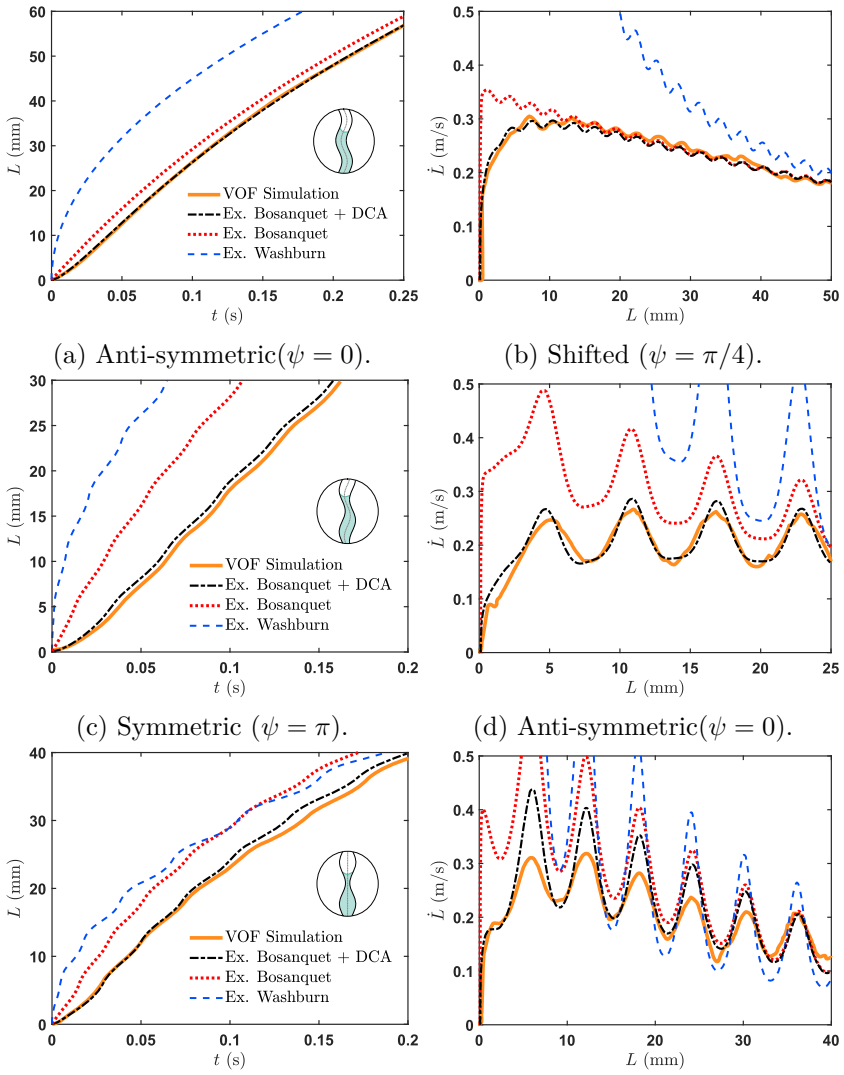

(a) Anti-symmetric($\psi = 0$). (b) Shifted ($\psi = \pi/4$).

(c) Symmetric ($\psi = \pi$). (d) Anti-symmetric($\psi = 0$).

(e) Shifted ($\psi = \pi/4$). (f) Symmetric ($\psi = \pi$).

Figure 4.4: Results of the wicking length variations with time ($L(t)$, left panels, (a),(c), and (e)) and the wicking rate with the meniscus position ($\dot{L}(L)$, right panels, (b),(d), and (f)) in lower Reynolds range ($\mathrm{Re} \sim 50 - 70$) for the extended Washburn (dashed blue lines), extended Bosanquet (with $\gamma(t) = 1$, dotted red lines), and extended Bosanquet + DCA (Equation 3.21, dot-dashed black lines) compared against VOF simulations (continuous orange lines) in three sinusoidal capillaries, (a) case 4, anti-symmetric ($\psi = 0$), (c) case 5, shifted at $\psi = \pi/4$, (e) case 6, symmetric ($\psi = \pi$).

Table 4.1: The specifications of 6 cases studied and verified against VOF simulation is Figures 4.3 and 4.4. The geometrical parameters (h_0^x, a^x, λ^x, and ψ) are non-rectified and [–] denotes a non-dimensional parameter. As Reynolds and Dean numbers are time-dependent, their temporal average in the interval of $t_v < t < 2\,t_v$ is represented as $\overline{\mathrm{Re}}$ and $\overline{\mathrm{De}}$. Please note that the reported $\overline{\mathrm{Re}}$ is calculated after the application of the viscous correction (ξ). However, the viscous correction itself is obtained based on $\overline{\mathrm{Re}}$ when no correction is applied. H is the *ad hoc* DCA constant.

Case	**Results**	**Type**	h_0^x (mm)	a^x (mm)	λ^x (mm)	ψ (rad)	$\overline{\mathrm{Re}}$ [–]	$\overline{\mathrm{De}}$ [–]	Oh $\times 10^{-3}$[–]	ξ [–]	H (mm)
1	Figure 4.3(a)	Anti-symmetric	0.30	0.20	2	0	37.8	29.0	5.04	1.00	200
2	Figure 4.3(c)	Shifted	0.30	0.15	2	$\pi/4$	36.2	24.4	4.94	1.00	250
3	Figure 4.3(e)	Symmetric	0.30	0.10	2	π	31.7	0	4.83	1.00	300
4	Figure 4.4(a)	Anti-symmetric	1.00	0.30	6	0	69.5	42.9	2.70	0.98	900
5	Figure 4.4(c)	Shifted	1.00	0.25	6	$\pi/4$	56.7	31.2	2.68	0.71	3000
6	Figure 4.4(e)	Symmetric	1.00	0.15	6	π	52.0	0	2.65	0.65	1400

4.3.2 Higher Reynolds Results

We now discuss the remaining Cases $4-6$, which presented higher Reynolds numbers (Re$\sim$ $50-70$). Here, it is worth mentioning that the Hagen–Poiseuille correction has to be used, and the coefficients were described in Table 4.1 along with other geometrical and non-dimensional numbers. Figure 4.4 shows wicking length *vs.* time and wicking rate *vs.* position results for Cases $4-6$.

Similar to the previous cases, the VOF solution and the Ex. Bosanquet + DCA model are in very close agreement with each other. The meniscus length differences between these two techniques are less than 2%, as can be seen in the left panels of Figure 4.4. When the wicking length behavior was examined, we also found an excellent agreement for Cases 4 and 5, while for Case 6, larger differences appeared. These differences diminished with the undulation of the channel and were almost zero at t = 40 s. These differences are detailed discussed in Section 4.4. Nevertheless, these differences in the wicking rate did not significantly affect the wicking length, which was predicted within a 2% error compared to VOF. Both Ex. Bosanquet and Ex. Washburn solutions have much larger discrepancies than VOF, which were attributed to the same reasons as in Cases 1-3.

Overall, while all solutions capture fluctuations in the wicking rate and wicking length due to the geometrical features of the channels, differences exist due to the different approximations and considerations in the governing equations. At the early stages of the wicking, it has been shown that inertial effects and the dynamic contact angle are more critical to predict the wicking length *vs.* time accurately. Remarkably, the Ex. Bosanquet + DCA model captures all features of the VOF simulations while requiring only modest computational power.

4.3.3 Effect of Gravity

Having analyzed the proposed solutions in capillaries with intricate geometries, we now study the solution under the effect of gravitational forces. To this end, we took the capillarity geometry used in Case 5 and detailed it in Table 4.1. Figure 4.5 shows the results of the extended Bosanquet equation compared against VOF simulations in the wicking of water with a zero and downward 9.81 $\mathrm{m{\cdot}s^{-2}}$ gravitational acceleration in the same geometry as in case 5 in Table 4.1.

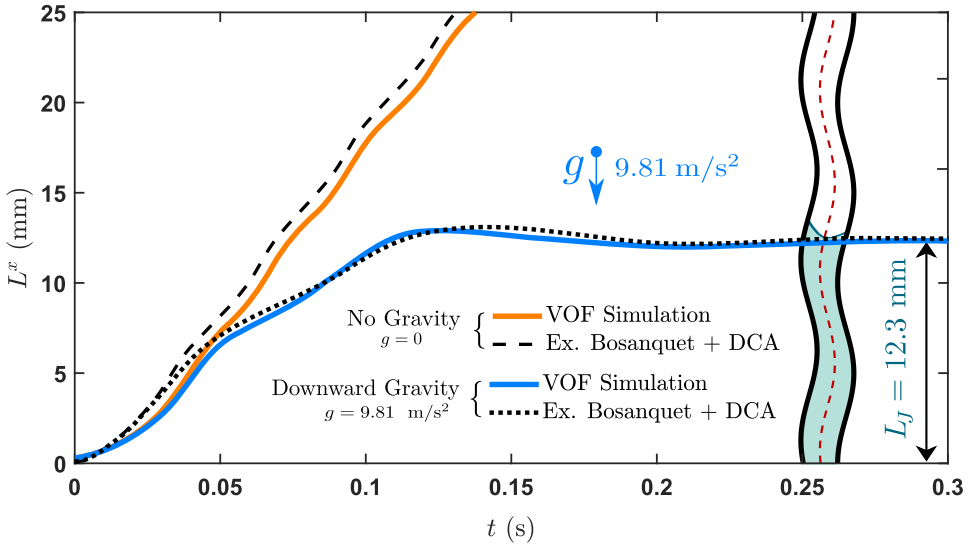

Figure 4.5: The effect of gravity on the capillary rise of water (with aforementioned properties) in a tortuous and corrugated channel (case 5 in Table 4.1, Figure 4.4b, schematically shown with a red, dashed centerline). Two cases with the same geometry are represented with a downward ($g = 9.81\ \mathrm{m \cdot s^{-2}}$) and zero gravity. The case with the downward gravity achieves equilibrium at the Jurin's height ($L_J = 12.3$ mm, where $P_c = P_g$) after slight gravitational oscillations. The Ex. Bosanquet equation + DCA (Equation 3.21) is shown in black dashed and dotted lines while the results of the VOF simulations are represented in solid, colored lines. Oh $= 2.68 \times 10^{-3}$, Bo $= 0.139$.

The meniscus height progression, L^x, as a function of time is depicted in Figure 4.5 for the two cases. The case with downward gravity ($g = 9.81$ m·s^{-2}), plateaus at the Jurin's height ($L_J = 12.3$ mm for both solutions) after slight gravitational oscillations with an overshoot of $L^x_{\max}/L_J = 0.05$. The low ratio of Oh/Bo $= 0.02 \ll 1$ describes the dominance of the viscous forces and rapid damping of gravitational oscillations around Jurin's height. Oscillations can be seen for both VOF and extended Bosanquet solutions when gravity went downward.

Gravity acts like a body force, i.e., the weight of the body of the wicking liquid. However, it does not appear so in the obtained ODE (as opposed to Lei *et al.* formulation [72]), for the pressure forces of the walls are a function of the weight of the body of the liquid. We concluded that the effect of gravity shows up as the hydrostatic pressure (P_g) in the governing ODE (Equation 3.19). This effect also means that when the dynamic pressure terms (viscous and inertial) are absent, the capillary and hydrostatic pressure balance out, yielding the static equilibrium. Since the hydrostatic pressure is a function of projection of the wicking length on the direction of gravitational acceleration ($P_g = \rho g L^x$).

4.3.4 Tubular Geometries

Thus far, the 2D channel geometry formulations represented in Equation 3.21 are verified with our VOF simulations. Similarly, this is also necessary to our 3D (tubular) formulation, delineated in Equation 3.22. In this regard, we would like to compare the interface tracking results for water flowing in a stepped-wall tube obtained by Erickson *et al.* [70] with our theoretical solution for such an irregular tube. Figure 4.6(a) shows the capillary rise of a diverging-converging and a converging-diverging stepped-wall tube and compares the extended Erickson *et al.*'s interface tracking solutions against extended Washburn and extended Bosanquet solutions (no dynamic contact angle included). The points where the extended Washburn and Bosanquet solutions cross each other are magnified in the Figure 4.6(b) I and II.

Figure 4.6(b) III shows where inertial (extended Bosanquet) and non-inertial (extended Washburn) for both tubes meet at the same length ($L = 86.1$ mm) but at different times. The inertial solution (extended Bosanquet) arrives at this length sooner (50.3 s), followed by the Erickson *et al.*'s interface tracking solution (51.8 s), and then that of extended Washburn, excluding inertia

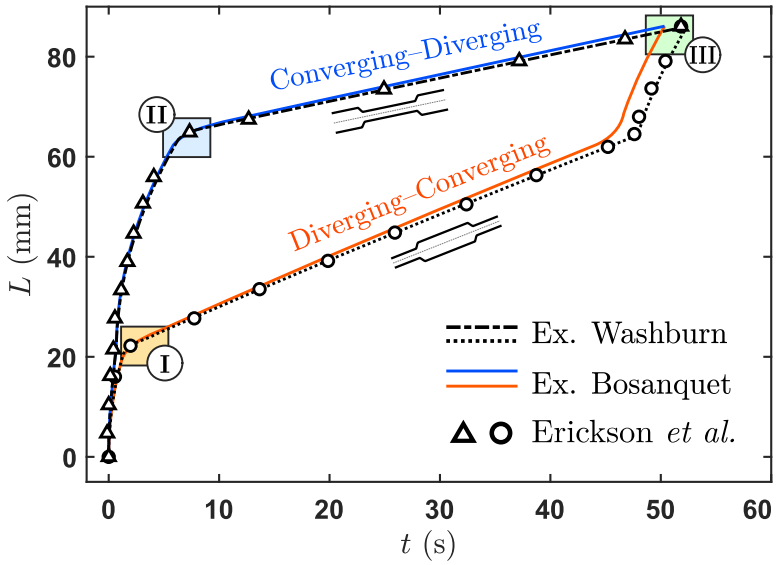

(a) Comparison of the results with Erickson *et al.* (2002)

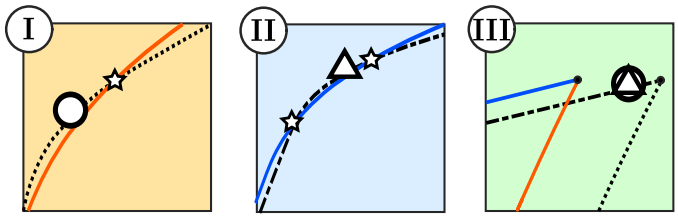

(b) Three magnified regions of interest

Figure 4.6: (a) Comparison between the extended Bosanquet equation and extended Washburn equation (no inertia) and the results obtained by Erickson *et al.* [70] using interface-tracking solution on a pair of symmetric converging-diverging and diverging-converging stepped-tubes. Three special regions of interest (I, II, and III) are magnified in (b) to clearly distinguish between different sets of results. The flow parameters are given as $r_{\max} = 50$ μm, $r_{\min} = 25$ μm, $\sigma = 0.03$ N·m^{-1}, $\theta = 30°$, $\eta = 0.001$ kg·m^{-1}·s^{-1}, and $\rho = 1000$ kg·m^{-3}. The transition from one radius to another smoothly occurs with a 0.5° taper angle. The stars ($\star$) depict the points where inertial (Ex. Bosanquet, Equation 3.22 with $\gamma(t) = 1$) and non-inertial (Ex. Washburn, Eqaution 1.7b) solutions meet.

(52.4 s).

This behavior could seem counterintuitive, as the inertia might mistakenly be perceived as a hindering force. Although it is so at the beginning of the rise, when the wicking fluid is yet to develop velocity, inertia also increases the response time of the liquid when the viscous force grows stronger. This effect can be observed in Figure 4.6(b) I and II, for a diverging-converging and a converging-diverging stepped-wall tube, respectively. The sharper curve in the extended Washburn solutions is compared to a much smoother transition in the extended Bosanquet solution owing to the effect of inertia, resulting in faster meniscus progression of the meniscus of the inertial solution.

4.4 Discussion

We have presented the results and compared them against our VOF simulations and the literature. Although the solution to the proposed ODE (Equation 3.20) is in good agreement with the simulations, a level of discrepancy persists in most cases. These discrepancies are due to various phenomena inherently included in the VOF simulations but neglected in the theory, as our assumptions are similar to those of Bosanquet. These include the dynamic pressure drop at the bottom of the capillary, the effect of the depth of immersion (L^*), and the undeveloped velocity profile at the entrance. Other phenomena include the 2D or axisymmetric nature of the velocity field of the wicking liquid in the corrugated channels or tubes, which is simplified to a 1–D flow through the Hagen–Poiseuille equation in the theory, the violation of the no-slip condition and parabolic velocity distribution close to the meniscus, the changes in the shape of the meniscus, and the centripetal acceleration in tortuous ducts.

Nevertheless, the differences between the meniscus positions as a function of time were in excellent agreement between the extended Bosanquet equation and VOF simulations. In the absence of gravity, the differences were less than 2% for a wide range of channels with different geometries and exhibiting different Reynolds and Dean's numbers (see Table 4.1 for specific details). When gravity was present, we observed that Jurin's height was in excellent agreement between VOF and extended Bosanquet, and the two solutions presented oscillations in the meniscus height due to the interplay between inertial effects and viscous forces.

4.4.1 Dominant Forces during Capillary Rise

As discussed in the introduction, the dominant forces at play during the wicking do not stay the same. Equation 3.20 is the governing equation of the meniscus position ($L(t)$) consists of various terms, each representing the effect of a particular force during the capillary rise, i.e., inertial, viscous, capillary and gravity. It is now instructive to evaluate the evolution of these forces during the meniscus rise as a function of time. To show the dominance among the terms involved in the obtained ODE, we define a new function called the *total magnitude*, $\mathcal{M}(t)$, summing up the absolute values of all the acting terms,

$$\mathcal{M}(t) = \underbrace{|\mathcal{A}\,\ddot{L}(t) + \mathcal{B}\,\dot{L}^2(t)|}_{\text{inertia}} + \underbrace{|\mathcal{C}(t)\,\dot{L}|}_{\text{viscous}} + \underbrace{|\mathcal{G}(t)|}_{\text{gravity}} + \underbrace{|\mathcal{D}(t)|}_{\text{capillary}} . \tag{4.2}$$

Figure 4.7 shows the share of each term in the total magnitude ($\mathcal{M}(t)$) for a flat and a sinusoidal symmetric corrugated channel with the same width and wave amplitude of $a = 50$ μm and wavelength of $\lambda = 5$ mm, with and without the effect of a gravitational force ($g = 1\ \mathrm{m \cdot s^{-2}}$). Regardless of the geometry, at the onset of the capillary rise, the capillary and inertial terms are balanced, constituting half of the total magnitude each. The share of the viscous and gravity terms is negligible at this stage, for the wicking liquid has not yet developed any considerable velocity or height. Beginning around the capillary time scale ($t_c = \sqrt{\rho h^3/\sigma} \sim 0.004$ s), the share of the viscous term, which is linearly-dependent on the velocity, starts to grow. Here, the behavior starts to be different between flat and complex geometry channels. For flat channels, in the absence of gravity, the share of the viscous term increases as the effect of inertia fades out, and the system eventually arrives at a dynamic equilibrium between the capillary and viscous forces around the viscous time scale ($t_v = h^2/\nu \sim 1$ s), heralding a Washburn regime (see Figure 4.7(c)). Next, suppose the gravity is present (see Figure 4.7(a)). In that case, the share of the gravity term, being linearly-dependent on the wicking height (L^x), constantly increases till arriving at the Jurin's height (L_J), where it finally comes to an equilibrium with the capillary term after some possible oscillations, depending on the Oh/Bo ratio.

For the analyzed symmetric sinusoidal channel, when the viscous forces start to increase ($t_c = \sqrt{\rho \bar{h}^3/\sigma} \sim 0.004$ s), the geometrical undulations of the channel induced large fluctuations of the inertial forces, which oscillated between 20-80% of the total magnitude $\mathcal{M}(t)$. These fluctuations tended to vanish with time, especially under the effect of a gravitational

force (see Figure 4.7(b)). Even though the oscillations were significant, the moving average of the inertial forces followed closely the decaying behavior of the flat channel in the presence of gravity (cf. Figure 4.7(a) with Figure 4.7(b)). Both inertial and viscous forces vanished completely for the symmetric sinusoidal channel after $t = 1$ s, where the capillarity force and gravity force were balanced with each other.
In the absence of gravitational forces, we observe that in a long-term behavior, the share of the inertial term diminishes considerably differently in a flat and corrugated channel (cf. Figure 4.7(c) with Figure 4.7(d)). To measure this difference, we solved the capillary rise in both channels for 1000 s (much longer than shown in Figure 4.7), a very long time for the scale wicking phenomena. The share of the inertial term approximately diminished $\propto t^{-1}$ for the flat channel, whereas this was much slower for a corrugated channel. The moving average of the share of the inertial term declined at an approximate rate of $\propto t^{-1/3}$. Although there was almost no effect of inertia at $t = 10$ s in a flat channel, it was still present in a very slightly corrugated channel even after $t = 1000$ s ($\approx 2\%$ of the total magnitude). This despair behavior is attributed to the persistent change of the meniscus curvature and resulting velocity fluctuations (producing the inertial acceleration term, $\mathcal{A}\ddot{L}(t)$) in a corrugated channel even in very long-term behavior. This simple example illustrates the importance of inertial effects in corrugated and tortuous channels.

4.4.2 Jurin's Height

One important aspect of irregular capillaries is that contrary to regular capillaries, the Jurin's height (L_J) is not unique, for the non-linear equation of the capillary equilibrium may have multiple solutions. This non-uniqueness especially happens for periodically corrugated capillaries, in which the capillary pressure (P_c) undergoes periodic variations with the position of the meniscus and might have multiple solutions when equated with the linear distribution of the hydrostatic pressure, $P_g = \rho g L^x$. Figure 4.8 shows the variations of $P_c - P_g$ with the wicking length (L). When zero, the point is a state of static equilibrium, however, depending on the sign of the derivative of the function, the equilibrium could be either stable ($\frac{\mathrm{d}}{\mathrm{d}L}(P_c - P_g) < 0$, shown with up-pointing triangles) or unstable ($\frac{\mathrm{d}}{\mathrm{d}L}(P_c - P_g) > 0$, shown with down-pointing triangles). Based on Equation 3.19 when $\frac{\mathrm{d}}{\mathrm{d}L}(P_c - P_g) < 0$, the derivative of the dynamic terms has to be negative either, which implies a stable situation, and vice versa. This fact describes that Jurin's height is path-dependent in irregular capillaries, dependent on how the liquid arrives

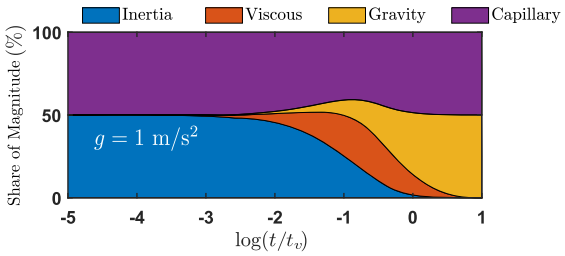

(a) A flat channel – with gravity

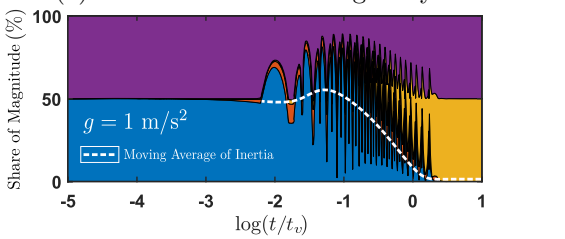

(b) A corrugated channel – with gravity

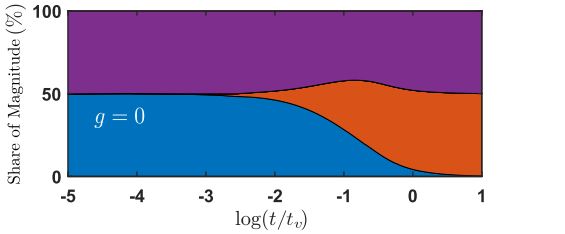

(c) A flat channel – no gravity

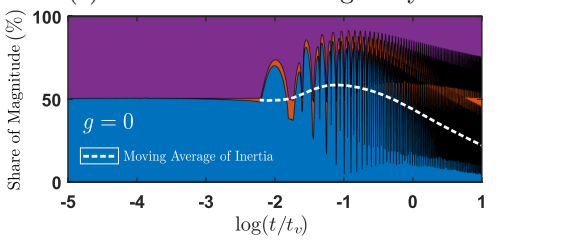

(d) A corrugated channel – no gravity

Figure 4.7: The share of terms in the total magnitude, $\mathcal{M}(t)$, plotted in a semi-logarithmic scale for the wicking of water in a channel over time (normalized by the viscous time scale t_v). (a) and (c) represent a flat channel with the width of 1 mm, while (b) and (d) show the share of terms for a sinusoidal symmetric corrugated channel with the same width and wave amplitude of $a = 50$ μm and wavelength of $\lambda = 5$ mm. The gravity is present in (a) and (b) ($g = 1$ m·s^{-2}), but not (c) and (d). The moving average of the inertial terms in the corrugated channel is drawn in white, dashed lines due to high-frequency oscillations.

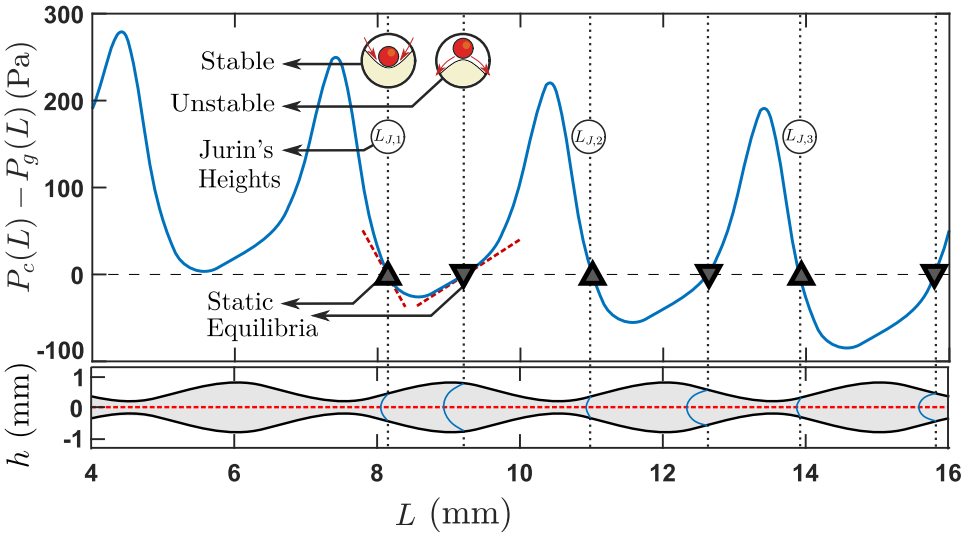

Figure 4.8: The multiple static equilibria (where $P_c = P_g$) plotted as a function of the meniscus position (L) for a sinusoidal symmetric channel shown at the bottom ($h_0^x = 1$ mm, $a_0^x = 0.3$ mm, $\lambda^x = 1$ mm, $\psi = \pi$). The stable (Jurin's heights) and unstable equilibria are presented with up-pointing and down-pointing triangles, respectively. The derivative of $P_c - P_g$ at the equilibria shown with red dashed line signifies stability once negative, and vice versa.

at each equilibrium candidate point. Depending on the relative strength of inertia (more accurately, the Oh/Bo ratio), the system might be forced out of the first equilibrium candidate (the smallest for the Jurin's height) and go to the next one. The system might skip or even come back to several equilibrium candidates during gravitational oscillations before coming to rest at the eventual Jurin's height.

Figure 4.9 depicts the effect of the dynamic viscosity (η) on the Jurin's height in a sinusoidal symmetric channel (Figure 4.9(c)) for a liquid with properties same as water except for its viscosity, which is subject to change. For high viscosities larger than the first *bifurication viscosity* ($0.00128 > \eta_b > 0.00127$ kg·m^{-1}·s^{-1}), the first static equilibrium ($L_{J,1} = 8.1$ mm) is the confluence of all solutions, while for the viscosity values lower than the first bifurcation viscosity, the meniscus comes to rest at the second stable equilibrium ($L_{J,2} = 11.0$ mm, Figure 4.9(a)). The curves fork off at $L = 9.2$ mm, which is an unstable equilibrium height, and even a small effect of inertia forces the meniscus out of the equilibrium. It was also observed that by narrowing the bifurcation viscosity band ($0.00128 > \eta_b > 0.00127$ kg·m^{-1}·s^{-1}) to more decimals, the bifurcation will be postponed, and the meniscus stays longer at the unstable equilibrium, however, eventually coming to rest to one of either nearby stable equilibria. Figure 4.9(b) shows the viscosities lower than $\eta = 0.00031$ kg·m^{-1}·s^{-1}, where the higher ratio of inertial to the viscous forces causes the meniscus to find eventual equilibrium at all three equilibria within the solution domain. The meniscus might leave and come back to several equilibria before coming to rest at the Jurin's height.

Table 4.2: Water properties at 15°C and 20°C [86]. As we were unable to find a source distinguishing between the contact angle for this 5°C temperature difference, we assumed $\theta = \pi/6$ for both cases. The geometry ($h_0^x = 1$ mm, $a_0^x = 0.27$ mm, $\lambda^x = 5$ mm, $\psi = \pi$) and the gravitational acceleration ($g = 9.81$ m $\cdot$ s^{-2}) are the same for both cases.

T	θ	σ	η	ρ
°C	rad	N·m^{-1}	kg·m^{-1}·s^{-1}	kg·m^{-3}
15	$\pi/6$	0.07348	0.001138	999.1
20	$\pi/6$	0.07273	0.001002	998.2

Figure 4.10 shows an interesting example where only a 5°C temperature difference causes the water (with properties given at 15°C and 20°C given

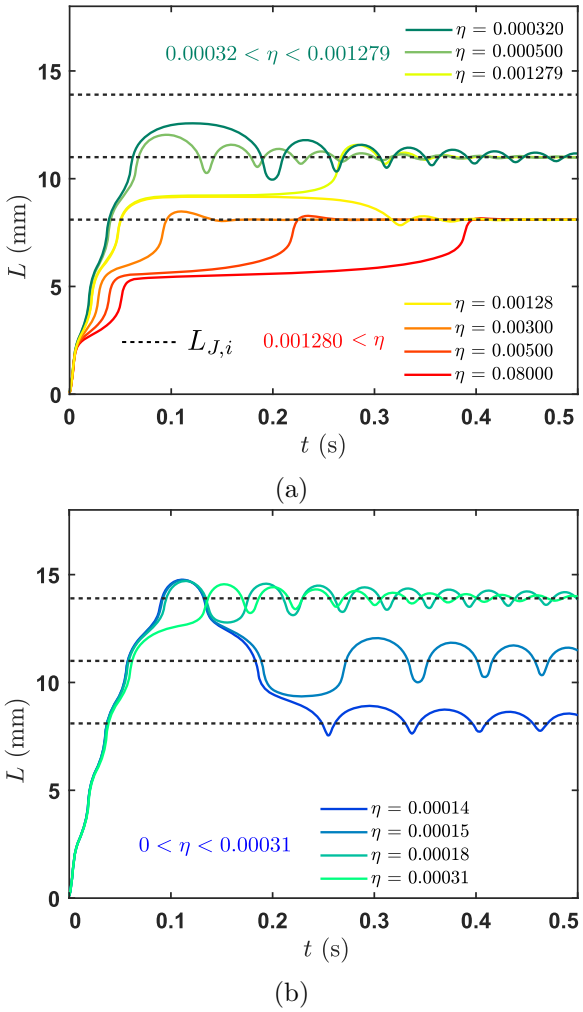

Figure 4.9: The effect of dynamic viscosity (η) on the Jurin's height in a sinusoidal symmetric channel ($h_0^x = 1$ mm, $a_0^x = 0.3$ mm, $\lambda^x = 1$ mm, $\psi = \pi$). Water has three static equilibria ($L_{J,1} = 8.1$ mm, $L_{J,2} = 11.0$ mm, and $L_{J,3} = 13.0$ mm) within the solution domain ($0 < L < 15$ mm) in this geometry. Changing the viscosity of water, (a) shows the Jurin's height for few sample viscosities in two intervals of $\eta > 0.00128$ kg·m^{-1}·s^{-1} (all eventually coming to rest at $L_{J,1}$) and $0.00127 > \eta > 0.00032$ kg·m^{-1}·s^{-1} (all coming to rest at $L_{J,2}$). The bifurication occurs between $0.00128 > \eta > 0.00127$ kg·m^{-1}·s^{-1}, where the curves part at an unstable equilibrium height, $L = 9.2$ mm. (b) covers the interval of $0.00031 > \eta > 0$ kg·m^{-1}·s^{-1}, showing multiple Jurin's height due to relative stronger effect of inertia. All viscosities are reported in kg·m^{-1}·s^{-1} in the legends.

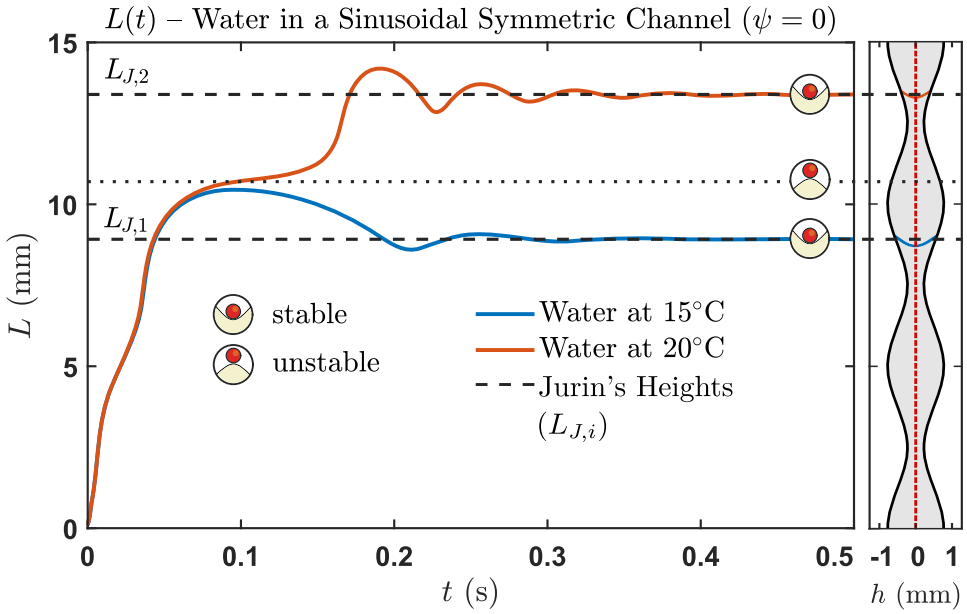

Figure 4.10: The capillary rise of water in a sinusoidal symmetric channel ($h_0^x = 1$ mm, $a_0^x = 0.27$ mm, $\lambda^x = 5$ mm, $\psi = \pi$) at two different temperatures (15°C and 20°C, properties given in Table 4.2). Three static equilibria (where $P_c = P_g$) exist in the solution interval, two of the being stable and referred to as the Jurin's height ($L_{J,1} = 8.9$ mm, $L_{J,2} = 13.4$ mm), and one being unstable ($L = 10.7$ mm). The small difference in water properties just by a 5°C temperature causes the meniscus to eventually come to rest in different stable equilibria.

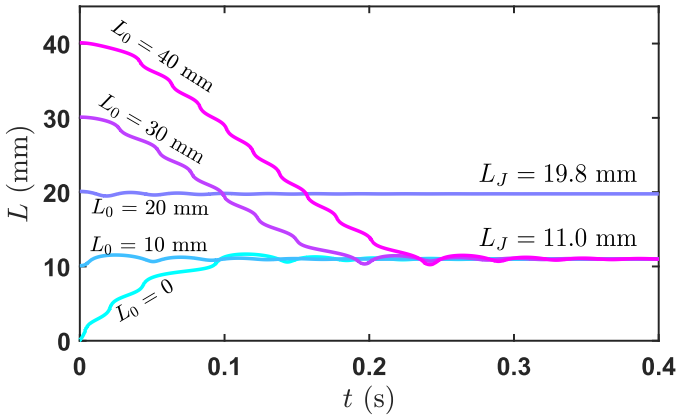

Figure 4.11: The effect of the initial condition (L_0) on the the Jurin's height of water in a sinusoidal symmetric channel ($h_0^x = 1$ mm, $a_0^x = 0.3$ mm, $\lambda^x = 1$ mm, $\psi = \pi$) which shows the main attractor is $L_J = 11$ mm while other stable equilibria may also eventually become the Jurin's height when the initial condition is chosen close to them ($L_0 = 20$ mm $\rightarrow L_J = 19.8$mm).

in Table 4.2) to eventually arrive at different equilibria ($\sim 50\%$ difference in height).

The solution is also highly sensitive to the initial conditions. In Figure 4.11, the initial position of the meniscus (L_0) is subject to change, while $\dot{L}_0 = 0$ for all cases. Having nine stable equilibria in total, most of the cases are attracted by $L_{J,2} = 11$ mm, thereby being referred to the *main attractor* among the Jurin's heights. Other Jurin's heights may only be achieved when the meniscus is initially located close enough to them. The last potential Jurin's height ($L_{J,9} = 31.52$ mm) may only be achieved as long as L_0 is chosen very close to it. If $L_0 = 31.5$ mm, the meniscus eventually comes to rest at $L_{J,9} = 31.52$ mm but even slightly deviated cases such as $L_0 = 30$ mm and $L_0 = 40$ mm considerably fall down and eventually find equilibrium at $L_{J,2} = 11$ mm.

Owing to the non-linear dynamics, solving the transient behavior of capillarity is necessary and is the only way the ture static equilibrium can be determined for an irregular capillary. Thus, in contrast to flat channels (Equation 1.2a) or simple tubes (Equation 1.2b), no single Jurin's height solution

can necessarily be presented for irregular capillaries. To guide the system into the desired equilibrium, one may change the viscosity. Higher viscosities strongly damp the gravitational oscillations and force the meniscus to come to rest at the first point of equilibrium, while low viscosities allow the meniscus to explore higher equilibria. As mentioned before, the meniscus might even fall again to lower equilibria and eventually come to rest at a lower point of equilibrium.

The effects of capillary hysteresis (i.e., the wetting history of the walls) could play a prominent role. However, this falls outside the scope of this work. Nevertheless, it is deemed to be a potential candidate for future avenues to explore.

Chapter 5

Conclusions and Future Work

We derived a governing ODE (Equation 3.20) for capillary flow in corrugated and tortuous channels (Equation 3.21) and tubes (Equation 3.22) including the effects of inertia, which was not rigorously investigated for geometrically irregular capillaries thus far.

The governing equation was found using a rectification procedure based on the Voronoi segmentation algorithm that converts tortuous channels or tubes to their rectified, symmetric counterpart. In addition, a correction of the extended Hagen–Poiseuille equation (Equation 1.5) was also introduced to accurately predict the flow rate in high Reynolds number and highly corrugated channels. It was found that, contrary to flat channels where inertial effects decay $\propto t^{-1}$, corrugated channels showed a much slower decay $\propto t^{-1/3}$. This behavior is due to the geometrical changes of the channel's profile, which produces changes in the contact angle and capillary pressure as the meniscus rises. Overall, the inertial solution found with Equation 3.20 was in excellent agreement with VOF simulations, experimental data, and other published works found in the literature.

The extended Hagen–Poiseuille equation (Equation 1.5) proved to fail to accurately predict the flow rate in high Reynolds number and highly corrugated ducts, when the uni-directional flow assumption breaks down, thereby necessitating a viscous correction factor to account for neglected viscous tractions on the walls resulting from a 2D or 3D flows in high Reynold results (Figure 4.4). One may draw this important conclusion that the wicking length (L) will be independent of tortuosity or inclination of the duct in the absence of gravity, as $\cos\alpha(s)$ only appears in the gravity term.

One of the major findings of this study is the role that inertia plays in determining Jurin's height at which the meniscus eventually comes to rest, which may not be understood, excluding the effect of inertia. Although being fully

deterministic, it was shown that the problem could heavily be dependent on the initial conditions and the dynamic parameters (such as viscosity, η), which do not show up at the static equilibrium formula (Equation 3.23) themselves. An exemplary case of wicking water in a sinusoidal corrugated channel demonstrated that the change of water properties resulting from a 5°C temperature change might entirely switch the eventual Jurin's height to another stable equilibrium.

In summary, the most important points include:

- Tortuous capillaries (those with a curved centerline) could be *rectified* into their symmetric counterpart and then be analyzed similarly, as long as the flow is unidirectional, i.e., in the absence of secondary flows. The threshold of the emergence of secondary flows is determined by Dean's number (De).
- Contrary to flat capillaries, irregular capillaries may have multiple static equilibria, either stable or unstable, and only through the inclusion of inertia, higher equilibria may be achieved. Non-inertial formulations necessarily force the meniscus to come to rest at the first static equilibrium.
- The Jurin's height is *path-dependent* and the dynamics of wicking process must be solved to determine the eventual equilibrium height.
- The Jurin's height could be very sensitive to the properties of the liquid and the capillary duct, also the initial conditions and the wetting history of the walls. Higher viscosities were shown to damp the gravitational oscillations and enforce lower static equilibria owing to higher energy dissipation.
- The effect of inertia stays longer at play in irregular geometries with periodic wall angle variations compared to flat geometries.

The extended Bosanquet equation (Equation 3.20) obtained in this paper could serve as a prospective tool to investigate various phenomena, and review the findings of previous studies that may now reveal more interesting aspects once the inertia is taken into account, e.g., the effect of the corrugation amplitude, the tortuosity, various wall profiles, and the effective diffusion of irregular capillaries.

Elastocapillarity is a prospective avenue to explore, as elastic capillary walls

undergo geometric deformations that convert even regular capillaries to irregular after the initiation of wicking. It may also shed light on the complex nature of wicking dynamics in deformable and inflatable media, such as paper towels and other bioproducts. However, the extended Bosanquet equation derived in this paper is not eligible to study elastocapillary problems, as we neglected the temporal changes of the capillary walls. A new version of this equation may be obtained considering time-dependent wall profiles ($h = h(x,t)$ or $r = r(x,t)$).

Future studies may also include studying wicking in rough, porous media considering the effect of inertia, the implementation of the dynamic pressure drop at the mouth of the capillary, which is not considered in this study, the effects of hysteresis (or the wall's wetting history), non-Newtonian inertial capillary flows, tubular capillaries with their axes as space curves, such as helical capillaries, and the experimental studies of multiple static equilibria and the eventual Jurin's height.

Bibliography

[1] R. Masoodi and K. M. Pillai. *Wicking in Porous Materials: Traditional and Modern Modeling Approaches*. CRC Press, oct 2012.

[2] P. G. de Gennes, F. Brochard-Wyart, and D. Quéré. *Capillarity and Wetting Phenomena: Drops, Bubbles, Pearls, Waves*. Springer New York, New York, NY, 2004.

[3] M. H. Zimmermann. *Xylem Structure and the Ascent of Sap*. Springer, 1983.

[4] A. R. Parker and C. R. Lawrence. Water capture by a desert beetle. *Nature*, 414(6859):33–34, 2001.

[5] P. Comanns. Erratum: Passive water collection with the integument: mechanisms and their biomimetic potential. *The Journal of Experimental Biology*, 221, 2018.

[6] D. Gurera and B. Bhushan. Passive water harvesting by desert plants and animals: lessons from nature. *Philosophical Transactions of the Royal Society A: Mathematical, Physical and Engineering Sciences*, 378(2167):20190444, 2020.

[7] W. Kim, F. Peaudecerf, M. W Baldwin, and J. W. M. Bush. The hummingbird's tongue: a self-assembling capillary syphon. *Proceedings of the Royal Society B: Biological Sciences*, 279(1749):4990–4996, 2012.

[8] W. Kim and J. W. M. Bush. Natural drinking strategies. *MIT web domain*, 2012.

[9] R. A. Samy, D. George, and A. K. Sen. Bio-inspired liquid transport via elastocapillary interaction of a thin membrane with a liquid meniscus. *Soft Matter*, 13(38):6858–6869, 2017.

[10] G. L. MacLean. Water transport by sandgrouse. *Bio Science*, 33(6):365–369, 1983.

[11] T. W. Kim and B. Bhushan. The adhesion model considering capillarity for gecko attachment system. *J. R. Soc. Interface*, (5):319–327, 2008.

[12] H. E. Jeong, S. H. Lee, P. Kim, and K. Y. Suh. High aspect-ratio polymer nanostructures by tailored capillarity and adhesive force. *Colloids and Surfaces A: Physicochemical and Engineering Aspects*, 313-314:359–364, 2008.

[13] S. Kar, T. K. Maiti, and S. Chakraborty. Capillarity-driven blood plasma separation on paper-based devices. *Analyst*, 140(19):6473–6476, 2015.

[14] M. Sneha Maria, P. E. Rakesh, T. S. Chandra, and A. K. Sen. Capillary flow-driven microfluidic device with wettability gradient and sedimentation effects for blood plasma separation. *Scientific Reports*, 7(January):1–12, 2017.

[15] H. Wu, C. Shi, Q. Zhu, Y. Li, Z. Xu, C. Wei, D. Chen, and X. Huang. Capillary-driven blood separation and in-situ electrochemical detection based on 3D conductive gradient hollow fiber membrane. *Biosensors and Bioelectronics*, 171(September 2020):112722, 2021.

[16] A. R. Pries, D. Neuhaus, and P. Gaehtgens. Blood viscosity in tube flow: Dependence on diameter and hematocrit. *American Journal of Physiology - Heart and Circulatory Physiology*, 263(6 32-6), 1992.

[17] S. Kim, Y. I. Cho, A. H. Jeon, B. Hogenauer, and K. R. Kensey. A new method for blood viscosity measurement. *Journal of Non-Newtonian Fluid Mechanics*, 94(1):47–56, 2000.

[18] M. Kvick, M. D. Martinez, D. R. Hewitt, and N. J. Balmforth. Imbibition with swelling: capillary rise in thin deformable porous media. *Physical Review Fluids*, 2(7):1–19, 2017.

[19] M. Mirzajanzadeh, V. S. Deshpande, and N. A. Fleck. Water rise in a cellulose foam: by capillary or diffusional flow? *Journal of the Mechanics and Physics of Solids*, 124:206–219, 2019.

[20] J. P. Singh and B. K. Behera. Performance of terry towel - a critical review (part I): Water absorbency. *Journal of Textile and Apparel, Technology and Management*, 9(1):1–14, 2014.

[21] Z. Tavassoli, R. W. Zimmerman, and M. J. Blunt. Analytic analysis for oil recovery during counter-current imbibition in strongly water-wet systems. *Transport in Porous Media*, (58):173–189, 2005.

[22] W.H. Green and G. A. Ampt. Study on soil physics. *J. Agric. Sci*, 4 (1):1, 1911.

[23] F. A. L. Dullien. Capillarity in porous media. In *Porous Media: Fluid Transport and Pore Structure*, pages 5–74. Academic Press, 1979.

[24] H. Czachor. Modelling the effect of pore structure and wetting angles on capillary rise in soils having different wettabilities. *Journal of Hydrology*, 328(3-4):604–613, 2006.

[25] L. Courbin, E. Denieul, E. Dressaire, M. Roper, A. Ajdari, and H. A. Stone. Imbibition by polygonal spreading on microdecorated surfaces. *Nature Materials*, 6(9):661–664, 2007.

[26] Y. V. Najdich, I. I. Gab, V. A. Evdokimov, D. I. Kurkova, and T. Stetsyuk. Shape of a liquid surface and capillary phenomena under reduced or zero gravity. *Poroshkovaya Metallurgiya*, 43(3-4):70–79, 2004.

[27] M. M. Weislogel. Compound capillary rise. *Journal of Fluid Mechanics*, 709:622–647, 2012.

[28] T. Tarnev, S. Cychy, C. Andronescu, M. Muhler, W. Schuhmann, and Y. T. Chen. A Universal Nano-capillary Based Method of Catalyst Immobilization for Liquid-Cell Transmission Electron Microscopy. *Angewandte Chemie - International Edition*, 59(14):5586–5590, 2020.

[29] A. Lundberg, J. Örtegren, E. Alfthan, and G. Ström. Paper-ink interactions: Microscale droplet absorption into paper for inkjet printing. *Nordic Pulp and Paper Research*, 26(1):142–150, 2011.

[30] N. O. Young. Capillary Lubrication. *Nature*, 216(63):1246, 1967.

[31] E. Elizalde, R. Urteaga, R. R. Koropecki, and C. L. Berli. Inverse Problem of Capillary Filling. *Physical Review Letters*, 112(13):134502, 2014.

[32] T. Young. An essay on cohesion of fluids. *Philosophical Transactions of the Royal Society of London*, 95:65–87, 1805.

[33] P. S. M. de Laplace. Traité de mécanique céleste. *Chez J.B.M. Duprat*, VII, 1805.

[34] J. Jurin. An account of some experiments shown before the royal society; with an enquiry into the cause of some of the ascent and suspension of water in capillary tubes. *Philosophical Transactions of the Royal Society of London*, 30:739747, 1718.

[35] J. Jurin. An account of some new experiments, relating to the action of glass tubes upon water and quicksilver. *Philosophical Transactions of the Royal Society of London*, 30:10831096, 1719.

[36] J. M. Bell and F. K. Cameron. The flow of liquids through capillary spaces. *Journal of Physical Chemistry*, 10(8):658–674, 1905.

[37] E. W. Washburn. The Dynamics of Capillary Flow. *The Physical Review*, VI(c):273–283, 1921.

[38] V. R. Lucas. Überber das zeitgesetz des kapillaren aufstiegs von flüssigkeiten. *Kolloid Zeistschrift*, 23:1522, 1906.

[39] M. Reyssat, L. Courbin, E. Reyssat, and H. A. Stone. Imbibition in geometries with axial variations. *Journal of Fluid Mechanics*, 615:335–344, 2008.

[40] D. Quéré. Inertial capillarity. *EPL (Europhysics Letters)*, 39(5):533, 1997.

[41] K. G. Kornev and A. V. Neimark. Spontaneous Penetration of Liquids into Capillaries and Porous Membranes Revisited. *Journal of Colloid and Interface Science*, 235(1):101–113, 2001.

[42] C. H. Bosanquet. On the flow of liquids into capillary tubes. *Phil. Mag.*, 45:525531, 1923.

[43] M. Stange, M. E. Dreyer, and H. J. Rath. Capillary driven flow in circular cylindrical tubes. *Phys. Fluids*, 15(9):2587–2601, 2003.

[44] S. Das and S. K. Mitra. Different regimes in vertical capillary filling. *Physical Review E*, 87(6):63005, 2013.

[45] M. Dreyer, A. Delgado, H. J. Path, T. W. Gyves, and T. F. Irvine. Capillary rise of liquid between parallel plates under microgravity. *Journal of Colloid And Interface Science*, 163(1):158–168, 1994.

[46] N. Fries and M. Dreyer. The transition from inertial to viscous flow in capillary rise. *Journal of Colloid and Interface Science*, 327(1):125–128, 2008.

[47] S. Das, P. R. Waghmare, and S. K. Mitra. Early regimes of capillary filling. *Physical Review E*, 86(6):67301, 2012.

[48] S. Chen, Z. Ye, L. Duan, and Q. Kang. Capillary driven flow in oval tubes under microgravity Capillary driven flow in oval tubes under microgravity. *Phys. Fluids*, 032111(December 2020), 2021.

[49] A. Ponomarenko, D. Quéré, and C. Clanet. A universal law for capillary rise in corners. *Journal of Fluid Mechanics*, 666:146–154, 2011.

[50] Y. Tian, Y. Jiang, J. Zhou, and M. Doi. Dynamics of Taylor rising. *Langmuir*, 35(15):5183–5190, 2019.

[51] J. Zhou and M. Doi. Universality of capillary rising in corners. *Journal of Fluid Mechanics*, 900(Doi), 2020.

[52] Ho-Young Young Kim and L. Mahadevan. Capillary rise between elastic sheets. *Journal of Fluid Mechanics*, 548:141–150, 2006.

[53] A. D. Gat and M. Gharib. Elasto-capillary coalescence of multiple parallel sheets. *Journal of Fluid Mechanics*, 723:692–705, 2013.

[54] B. Nasouri, B. Thorne, and G. Elfring. Dynamics of poroelastocapillary rise. *Journal of Fluids and Structures*, 85:220–228, 2019.

[55] J. Bico, B. Roman, L. Moulin, and A. Boudaoud. Elastocapillary coalescence in wet hair. *Nature*, 432(7018):690, 2004.

[56] J. Bico, É. Reyssat, and B. Roman. Elastocapillarity: When surface tension deforms elastic solids. *Annual Review of Fluid Mechanics*, 50(1):629–659, 2018.

[57] T. L. Staples and D. G. Shaffer. Wicking flow in irregular capillaries. *Colloids and Surfaces: Physicochemical and Engineering Aspects*, 204:477, 2001.

[58] J. C. Cai, B. M. Yu, M. F. Mei, and L. Luo. Capillary rise in a single tortuous capillary. *Chinese Physics Letters*, 27(5), 2010.

[59] L. Hathout and H. M. Do. Vascular tortuosity: A mathematical modeling perspective. *Journal of Physiological Sciences*, 62(2):133–145, 2012.

[60] N. Epstein. On tortuosity and the tortuosity factor in flow and diffusion through porous media. *Chemical Engineering Science*, 44(3):777–779, 1989.

[61] L. Shen and Z. Chen. Critical review of the impact of tortuosity on diffusion. *Chemical Engineering Science*, 62:3748–3755, 2007.

[62] J. Cai and B. Yu. A discussion of the effect of tortuosity on the capillary imbibition in porous media. *Transport in Porous Media*, 89(2):251–263, 2011.

[63] K. A. Polzin and E. Y. Choueiri. A similarity parameter for capillary flows. *Journal of Physics D: Applied Physics*, 36(24):3156–3167, 2003.

[64] W. B. Young. Analysis of capillary flows in non-uniform cross-sectional capillaries. *Colloids and Surfaces A: Physicochemical and Engineering Aspects*, 234(1-3):123–128, 2004.

[65] A. Shobeiri and M. Ponga. Dynamics of capillary rise in sinusoidal corrugated channels. *Progress in Paper Physics Seminar*, pages 6–9, 2020.

[66] B. Figliuzzi and C. R. Buie. Rise in optimized capillary channels. *Journal of Fluid Mechanics*, 731:142–161, 2013.

[67] J. B. Gorce, I. J. Hewitt, and D. Vella. Capillary imbibition into converging tubes: Beating Washburn's law and the optimal imbibition of liquids. *Langmuir*, 32(6):1560–1567, 2016.

[68] T. L. Bergman. Computational simulation of spontaneous liquid penetration and depression between vertical parallel plates. *Journal of Fluids Engineering*, 143(May):1–11, 2021.

[69] S. Pavuluri, J. Maes, and F. Doster. Spontaneous imbibition in a microchannel: analytical solution and assessment of volume of fluid formulations. *Microfluidics and Nanofluidics*, 22(8):0, 2018.

[70] D. Erickson, D. Li, and C. B. Park. Numerical simulations of capillary-driven flows in nonuniform cross-sectional capillaries. *Journal of Colloid and Interface Science*, 250(2):422–430, 2002.

[71] R. Chassagne, F. Dörfler, M. Guyenot, and J. Harting. Modeling of capillary-driven flows in axisymmetric geometries. *Computers and Fluids*, 178:132–140, 2019.

[72] J. Lei, Z. Xu, F. Xin, and T. J. Lu. Dynamics of capillary flow in an undulated tube. *Phys. Fluids*, 33(April):052109, 2021.

[73] J. Marston, G. Toyofuku, C. Li, T. Truscott, and J. Uddin. Drainage, rebound and oscillation of a meniscus in a tube. *Phys. Fluids*, 30(8):82103, 2018.

[74] A. O. Parry, C. Rascón, E. A. G. Jamie, and D. G. A. L. Aarts. Capillary emptying and short-range wetting. *Phys. Rev. Lett.*, 108:246101, 2012.

[75] F. M. White and J. Majdalani. Solutions to Newtonian-Flow Equations. In *Viscous Fluid Flow*, chapter 3. McGraw-Hill Education, 2021.

[76] S. Levine, J. Lowndes, E. J. Watson, and G. Neale. A theory of capillary rise of a liquid in a vertical cylindrical tube and in a parallel-plate channel. *Journal of Colloid And Interface Science*, 73(1):136–151, 1980.

[77] M. Germano. The Dean equations extended to a helical pipe flow. *Journal of Fluid Mechanics*, 203:289–305, 1989.

[78] P. M. Ligrani and R. D. Niver. Flow visualization of Dean vortices in a curved channel with 40 to 1 aspect ratio. *Phys. Fluids*, 31(12 , Dec. 1988):3605–3617, 1988.

[79] A. Clerici, S. Perego, and T. M. Melloni. A Set of GRASS GIS-Based Shell Scripts for the Calculation and Graphical Display of the Main Morphometric Parameters of a River Channel. *International Journal of Geosciences*, (7):135–143, 2016.

[80] A. Golly and J. M. Turowski. Deriving principal channel metrics from bank and long-profile geometry with the R package cmgo. *Earth Surf. Dynam*, (5):557–570, 2017.

[81] Y. Xiao, F. Yang, and R. Pitchumani. A generalized analysis of capillary flows in channels. *Journal of Colloid and Interface Science*, 298(2):880–888, 2006.

[82] C. L. Trabi, F. F.a Ouali, G. McHale, H. Javed, R. H. Morris, and M. I. Newton. Capillary penetration into inclined circular glass tubes. *Langmuir*, 32(5):1289–1298, 2016.

[83] Ansys® Academic Research Fluent Release 12.0. Help System, 6.2.2 Mesh Quality, 2009.

[84] F. G. Wolf, L. O. E. Santos, and P. C. Philippi. Capillary rise between parallel plates under dynamic conditions. *Journal of Colloid And Interface Science*, 344(1):171–179, 2010.

[85] H. Pehlivan. Experimental investigation of convection heat transfer in converging diverging wall channels. *International Journal of Heat and Mass Transfer*, 66:128–138, 2013.

[86] A. Dinçer and C. Zamfirescu. Appendix B: Thermophysical Properties of Water. In *Drying Phenomena: Theory and Applications*. John Wiley & Sons, Ltd, 2016.

Appendix A

Force Balance

The force balance projected along the centerline on a generic channel volume element with a 2D depth of b shown in details in Figure 3.1(c) is represented below, with a similar approach for a 3D, tubular geometry,

$$\begin{aligned} \mathrm{d}F_s &= bPh'\mathrm{d}s \ + 2b\tau\mathrm{d}s + Pbh \\ &\quad - b\,(P + \frac{\partial P}{\partial s}\mathrm{d}s)(h + h'\mathrm{d}s) - \ \rho bhg_s\mathrm{d}s \qquad \text{(2D)}, \qquad \text{(A.1a)} \\ \mathrm{d}F_s &= 2\pi Prr'\mathrm{d}s \ + 2\pi r\tau\mathrm{d}s + \pi Pr^2 \\ &\quad - \pi\,(P + \frac{\partial P}{\partial s}\mathrm{d}s)(r^2 + 2rr'\mathrm{d}s) - \pi\rho r^2 g_s\mathrm{d}s \quad \text{(3D)}, \qquad \text{(A.1b)} \end{aligned}$$

where $g_s = \cos\alpha(s)\, g$ is the projected gravitational acceleration along the centerline. Also note that a factor of $(\cos\beta)^{-1}$ which is multiplied by the shearing stress (τ) due to the surface inclination is canceled out by a $\cos\beta$ due to projection along the centerline.

Appendix B

Differential Element Stretch Rate

The equations represented in the ODE which consist the $\dot{\mathrm{d}}s$ term are investigated in this section. Since the flux velocity in the Reynolds transport theorem is written in absolute values, the differential arc-length element stretch rate ($\dot{\mathrm{d}}s$) is assumed zero everywhere except for the advancing meniscus frontier $s = L$, where $\dot{\mathrm{d}}s = \dot{L}$. The integral can be expanded as the summation of n equally spaced infinitesimal elements (Δx_i) shown in Figure B.1 where the integrand is evaluated at discrete points ($f(x_i)$), as follows,

$$\int_0^L f(x)\ \dot{\mathrm{d}}x = \lim_{n\to\infty} \Sigma_{i=1}^{n} f(x_i)\dot{\Delta x}_i \tag{B.1}$$

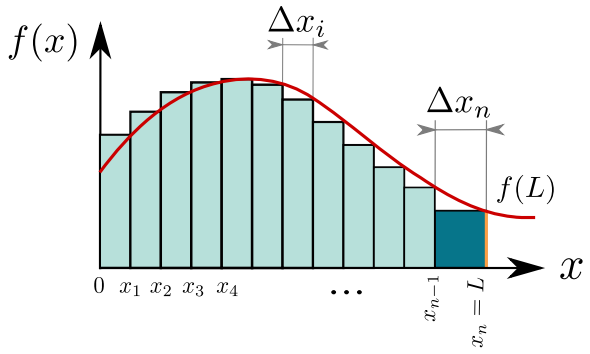

Figure B.1: The schematic of the integral discretization as the summation of finite elements.

where the following relation is held for the elements and the advancing integration limit $L(t)$,

$$\Sigma_{i=1}^{n} \Delta x_i = L, \tag{B.2a}$$

$$\Sigma_{i=1}^{n-1} \underbrace{\dot{\Delta x}_i}_{0} + \dot{\Delta x}_n = \dot{L}. \tag{B.2b}$$

Knowing that $x_i = x_{i-1} + \Delta x_i$ and $x_n = L$, considering the aforementioned conditions, substituting the equation above in Equation B.1,

$$\int_0^L f(x)\ \dot{\mathrm{d}}x = \lim_{n\to\infty}\left[\Sigma_{i=1}^{n-1}\, f(x_i)\underbrace{\dot{\Delta x_i}}_{0} + f(\underbrace{x_n}_{L})\underbrace{\dot{\Delta x_n}}_{\dot{L}}\right] = \dot{L}f(L). \tag{B.3}$$

This approach is similar to Leibniz integral rule ($\frac{\partial}{\partial t}\int_0^L f(s)\ \mathrm{d}s = \dot{L}\, f(L)$) and is responsible for differentiation with respect to varying integration limits. Neglecting this term results in the loss of the necessary nonlinear velocity term ($\dot{L}^2$) in flat channels or tubes (where $h'(s)$ or $r'(s)$ are respectively zero).

Appendix C

Dynamic Contact Angle

As the VOF solves the full Navier-Stokes equations for both phases and satisfies the Young-Laplace equation ($\Delta P = \kappa\sigma$) at the interface, the contact angle dynamically changes to satisfy the balance of forces at play. The dynamic evolution of the meniscus is graphically reproduced from the VOF simulations in Figure C.1, depicting the early stages of meniscus formation more clearly.

The flat interface is exposed to adhesive walls with $\theta = 30°$ at $t = 0$ (Figure C.1(a)). The outer surface of the capillary was made slippery with $\theta = 90°$ so that no delimiter is required. Shortly after the contact, the interface develops an angle with the wall (see Figure C.1(b)), inducing a curvature in the interface, thereby creating a pressure difference due to the Young-Laplace equation, which propagates towards the center of the tube (Figure C.1(c)-(f)), eventually forming a consistent curve, which later develops into a nearly circular curve when the meniscus starts to rise (Figure C.1(g)).

By way of contrast, in the extended Bosanquet equation (Equation 3.21 and 3.22), these complex effects are modeled with the DCA model, i.e.,

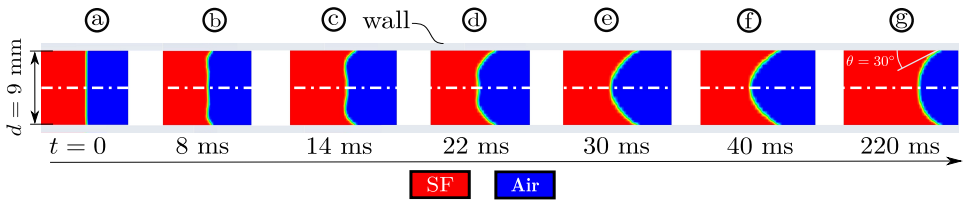

Figure C.1: Several snapshots from the early stages of meniscus formation in a silicone fluid (SF). The VOF results are compared to in the same problem as that of Stange *et al.* [43] in Figure 4.2 (case 2, shown with a continuous blue line, corresponding to a 9 mm diameter capillary). The capillary flow is simulated in a tube with $d = 9$ mm diameter using axial symmetry.

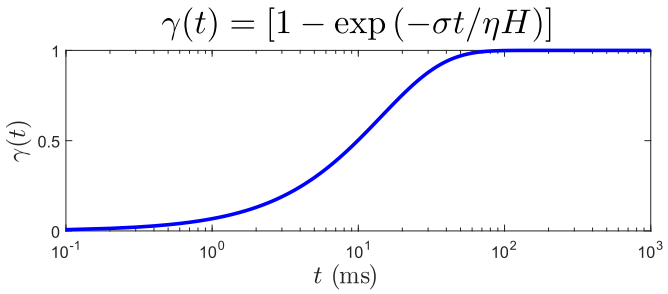

Figure C.2: The evolution of the dynamic contact angle model $\gamma(t)$ over time in a semi-logarithmic plot, for parameters $\sigma = 0.07$ N.m^{-1}, $\eta = 10^{-3}$ kg.m^{-1}.s^{-1}, and $H = 1$ m.

$\gamma(t) = [1 - \exp(-\sigma t/\eta H)]$ as described in [81] for flat geometries. This model basically assumes the meniscus has a constant curvature at all time, implying a circular configuration which is not true in reality (Figure C.1(b)-(f)). H is treated as an *ad hoc* constant in this study and is of length dimension. Figure C.2 shows the temporal evolution of a typical exponential saturation function of $\gamma(t)$.

Appendix D

Convergence Study

D.1 Mesh Convergence

To obtain a reliable mesh to avoid possible artifacts of the introduced spatial discretization a mesh convergence study is required. The mesh must be reined until the field of interest, i.e, the height of the meniscus $L(t)$ meets the convergence criterion which is chosen to be %1 in this study. Since the height of the meniscus is time dependent, it must be evaluated at a specific snapshot. To avoid long runs, $t = 0.5$ s has been designated to serve as this criterion. Table D.1 gathers the data regarding the mesh convergence in a typical capillary rise problem (Stange *et al.* [43]).

Table D.1: Mesh convergence study, four mesh configuration with ordered by the refinement increase tabulated with the height of the meniscus at $t = 0.5$ s in the case with $L^* = 10$ mm and $d = 4$ mm, shown in Figure 4.2 with a continuous orange line. The threshold of 1% dictates that M3 has enough accuracy. The error has been calculated relative to the previous stage, i.e., Err. $= |L_i - L_{i-1}|/L_{i-1}$. The mesh study is conducted in the domain D2 (see Table D.2).

Mesh	**Number of Elements**	L**(mm) at** $t = 0.5$ **s**	**Error (%)**
M1	$\approx 12.8 \times 10^3$	45.31	—
M2	$\approx 20.1 \times 10^3$	42.88	5.36
M3	$\approx 25.6 \times 10^3$	42.54	0.79
M4	$\approx 32.6 \times 10^3$	42.42	0.28

D.2 Domain Convergence

Having found the reliable mesh refinement (M3, Table D.1), a same study must be conducted for the distance of the introduced outer boundaries to the region of interest (the capillary). Table D.2 shows the details of the

domain convergence study for the same problem.

Table D.2: Domain convergence study, three domains with as same refinement as the obtained reliable mesh (M3, see Table D.1) in descending order indicated by the normalized distance to the centerline of the capillary (the ratio of the distance to the diameter of the tube), tabulated with the height of the meniscus at $t = 0.5$ s in the case with $L^* = 10$ mm and $d = 4$ mm, shown in Figure 4.2 with a continuous orange line. The threshold of 1% dictates that D3 has enough accuracy.

Domain	**Normalized Distance**	L**(mm) at** $t = 0.5$ **s**	**Error (%)**
D1	5	41.20	—
D2	10	42.54	3.25
D3	15	42.80	0.61

The time step must be chosen regarding each mesh configuration to satisfy the independence from the temporal discretization and the scaled residuals (which most preferably must fall to $\approx 10^{-5}$ when converged), however, the time step length of 5×10^{-6} s is usually sufficient.

As long as the dimensions of the capillary is relatively the same (such as the average width h_0^x and the ultimate wicking length), the same domain and mesh configurations may be used, however, for very different problem, all the steps must be taken the new conditions.